



Method Article

An optimization method for stochastic reconstruction from empirical data - A limestone rock strain fields study-case using digital image correlation data[☆]



Nathalia B. Guerra^{a,*}, Anderson V. Pires^a, Scott Matthews^c, Stefan Szyniszewski^d, Luiz C.M. Vieira Jr.^b

^a University of Campinas, Brazil

^b SGH: Simpson Gumpertz & Heger, United States

^c Permasense Ltd

^d Durham University, United Kingdom

ARTICLE INFO

Method name:

Stochastic Reconstruction of Limestone Rock Strain Fields Using Digital Image Correlation Data

Keywords:

Strain field
DIC
Metamodeling
Rock
Limestone
Correlation field
Gaussian process

ABSTRACT

Stochastic field reconstruction is a crucial technique to improve the accuracy of modern rock simulation. It allows explicit modelling of field conditions, often employed in uncertainty quantification analysis and upsampling and upscaling procedures. This paper presents a case-study of a framework for the stochastic reconstruction of rock's strain field using experimental data. The proposed framework is applied to a limestone outcrop in which the strain field is measured using Digital Image Correlation (DIC). Assuming that the strain fields of these rocks are well-represented by Gaussian random fields, we capitalize on the algorithms used for training Gaussian processes to estimate the correlation family and the parameters that best represent these fields. Although the spherical and exponential kernels often correspond to the best fit, our results depict that each field shall be analyzed separately and no general rule can be defined. We show that the method is versatile and can be employed in any measurable field reasonably represented by a Gaussian random field. Therefore, the present work aims to highlight the following topics:

- A study-case of stochastic strain field reconstruction aims to contribute to uncertainty quantification of rock experimental procedures.
- A stochastic minimization algorithm is presented to solve the maximum likelihood estimation to define the most suitable hyper-parameter: correlation length.
- The calculated hyper-parameters of a set correlation functions are presented to best reproduce the strain fields of a rock sample.

[☆] **Related research article** The present work applies different methods for the experimental and numerical analysis. However, we may cite the following reference as the main inspired study: J. Sacks, W.J. Welch, T.J. Mitchell, H.P. Wynn, Design and analysis of computer experiments, *Stat. Sci.* 4 (1989) 409–435. [24].

* Corresponding author.

E-mail address: nbatalha7@gmail.com (N.B. Guerra).

Specifications table

Subject area:	Engineering
More specific subject area:	Uncertainty quantification
Method Name:	Stochastic Reconstruction of Limestone Rock Strain Fields Using Digital Image Correlation Data
Name and reference of original method:	J. Sacks, W. J. Welch, T. J. Mitchell, H. P. Wynn, Design and analysis of computer experiments, Stat. Sci. 4 (1989) 409...435. [1] T. J. Santner, B. J. Williams, W. I. Notz, The Design and Analysis of Computer Experiments, Springer, New York, 2003. [2] S. N. Lophaven, H. B. Nielsen, J. S. ndergaard, DACE - a matlab kriging toolbox (2002) [3]
Resource availability:	Experiment can be replicated by following Appendix A. The optimization algorithm is available on the following Github link .

*Method details

Introduction

Full-field measurements, and non-destructive image techniques, have been widely applied to rock characterization [1–9]. Such studies evaluate material heterogeneity, fractures, strain field, and stochastic reconstruction. Strain field reconstruction from image data, in particular, may contribute to investigating rock behavior considering its heterogeneity in pore, strength, cracks, and so on. Stochastic reconstruction, or Gaussian process, significantly contributes to variable field generation in uncertainty quantification. Correlation functions, also known as kernels, are mathematical functions used to describe the correlation between variables. Such functions are fundamental in Gaussian processes and is used in numerical solutions such as metamodelling and geostatistics. Note that in stochastic processes and strain field reconstruction, [10,11], the squared exponential function is the most commonly used correlation function. According to Jidling et al. [12] “simple alternatives such as the squared exponential and the Matérn covariance functions should always be tried first, since they have shown to perform well in many applications.” However, based on experimental data, a method to identify the best kernel for Gaussian regression is important. The present work proposes a framework to determine the most suitable kernel and hyperparameters of strain fields for stochastic reconstruction. The present study contributes to the probabilistic analysis of rock mechanics and geomechanical modeling. Due to the framework’s versatility, it is possible to adjust it for other variables of interest, such as material properties, rock porosity, permeability, and others.

The method uses non-destructive methods such as Digital Image Correlation (DIC) to measure the strain field of rock samples under axial compression. Note that the DIC technique, also known as full-field measurement, can determine physical quantities, such as displacement, strain, and temperature variations [13]. Once strain does not change, it is possible to determine a field pattern variability through an optimization algorithm that searches for the best function hyperparameters and correlation function. Such parameters are computed by the Maximum Likelihood Estimation (MLE) method. Herein, the most suitable kernels and hyperparameters for the strain field of the tested limestone are provided, as well as the convergence of the optimization algorithm.

Materials and methods

Uniaxial compression tests of limestone samples were carried out, while DIC strain measurements were compiled. The strain data were post-processed using a metamodelling algorithm to evaluate the samples’ behavior and heterogeneity.

The methodology used herein is summarized as follows:

- i. Laboratory uniaxial compression test;
- ii. Full-field measurement of samples’ surface strain-data: DIC;
- iii. Metamodel to determine spatial correlation function and the hyperparameters of strain fields.

The framework depicted in [Fig. 1](#) describes the main steps of the proposed methodology.

Samples

The limestone rock used in the present study corresponds to an Italian travertine block. Limestone is largely composed of calcium carbonate (CaCO₃) which is mostly formed by the activity of seawater organisms, [14]. Cylindrical samples were extracted from the travertine block and cut into cubic samples. [Fig. 2](#) depicts the block cutting process and the final matrix samples with 4 × 3 objects with 6 × 6 × 6 cm dimension each. The cubic samples were the ones used in the DIC experiment. Note that sample porosity and permeability are not considered in this study.

DIC

As a non-contact method, DIC method stands on images recorded of an object that are stored digitally. records images of an object and stores them in digital form. The technique performs analysis to extract full-field shape, motion, and deformation measurements, [15]. The DIC method is widely used nowadays for full-field measurements. A software, underpinned by statistical computations, tracks movements of blocks of pixels to build up full-field deformation fields and resulting strain maps [16].

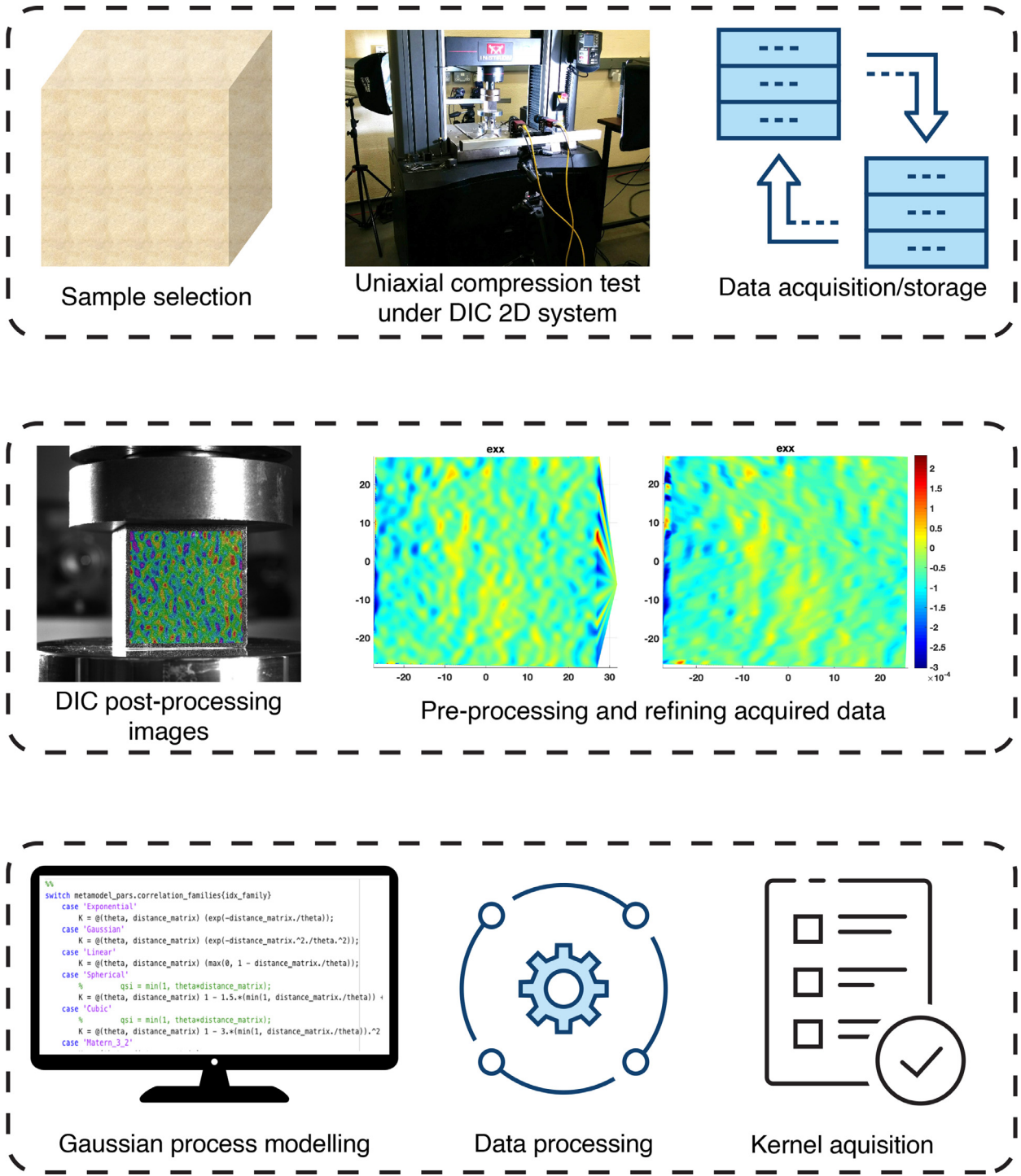


Fig. 1. Methodology framework.

The tested specimens were conducted by a stereo DIC system consisting of two 9-megapixel Allied Vision Technology Manta cameras, containing a 2/300 chip, with LINOS MeVis-C 1.6/35 lenses supplied by Correlated Solutions, Inc. According to Jones and Iadicola [17], the stereo DIC system corresponds to a 3D coordinate measurement of the surface, which is obtained by a minimum of two cameras oriented at a stereo-angle to perform 3D photogrammetry.

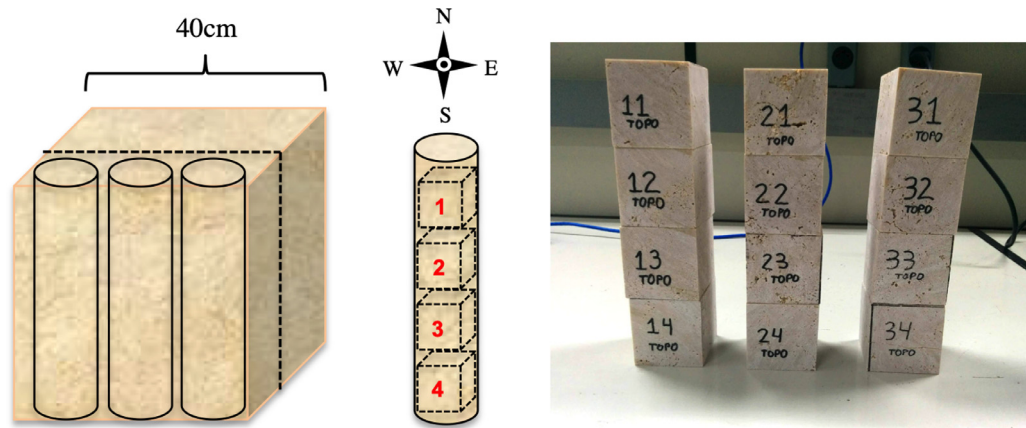


Fig. 2. Limestone block sample and cubic geometry after cutting.

The VIC-Snap software for setting up and calibrating the cameras was used, as well as the VIC-3D software for post-processing the images (Correlated Solutions, Inc. license both programs)

For the DIC process, the following main steps are required:

1. Speckling specimens' surface;
2. Set up the camera system;
3. Calibrate the cameras;
4. Run the experiment and take images at a set time range;
5. Post-process the DIC images.

Additional information regarding the limestone DIC experiment is documented in [Appendix A](#). Three samples were used for calibration: 14, 24, and 34. After calibration and adjustments, the remaining 9 cubic samples of 6 cm edge were tested. Keeping the material's response in the linear elastic regime is essential. Thus, to be conservative and avoid plastic deformation, the following cyclic load was designed for the 9 samples: load until 10 kN, unload until 2 kN, load until 35 kN, unload to 2 kN, load until 35 kN, unload until 2 kN, load until 35 kN and unload until 0 kN.

Data processing

The engineering strain fields of each sample are obtained from DIC post-processing: transverse (ϵ_{xx}), shear (ϵ_{xy}), and axial (ϵ_{yy}) strain fields. By selecting an area on the image taken from a specimen, DIC provides a strain tensor (ϵ) for each metric coordinate (x, y) inside the defined region. In order to maximize the covered field, all samples present a post-processing considering the selected area as presented in the example of [Fig. 3](#).

DIC result files can be large and a data cleaning method is necessary to improve computational cost. Thus, duplicate results and outliers are removed from data. [Fig. 4](#) depicts the data cleaning for Sample 21, which corresponds to the 14th image of front camera (System 1) in the experiment set. Parameters selection for the DIC image processing is described in [Appendix A](#). Also, one may note that a deep study of DIC noise minimization is out of the scope of this work.

Kriging

Historical context

Kriging is an interpolation method initially developed by Krige in the '50s [18] and mathematically formalized by Matheron in the '60s [19], who introduced the concept of variograms [20–23]. In the '80s, Sacks [24] proposed a new formulation for Kriging, relaxing the need for variograms, ultimately enabling its automation and making the method suitable for computational models. Currently, such technique is widely employed in the machine learning field under the name of Gaussian process modelling [25]. The method is more versatile than the original one as well as suitable for many problems with no or minimal modifications and user interactions. The code implemented for this project is available on GitHub.

Kriging basics

When employing Kriging, it is assumed that a physical quantity (respectively computational model), $\mathcal{M}(\mathbf{x})$, s.t., $\mathbf{x} \in D_{\mathbf{x}} \subset \mathbb{R}^M$, can be represented (respectively replaced) by a Gaussian process, described by [Eq. \(1\)](#).

$$\mathcal{M}(\mathbf{x}) = \mathbf{f}(\mathbf{x})^T \boldsymbol{\beta} + \sigma^2 Z(\mathbf{x}) \quad (1)$$

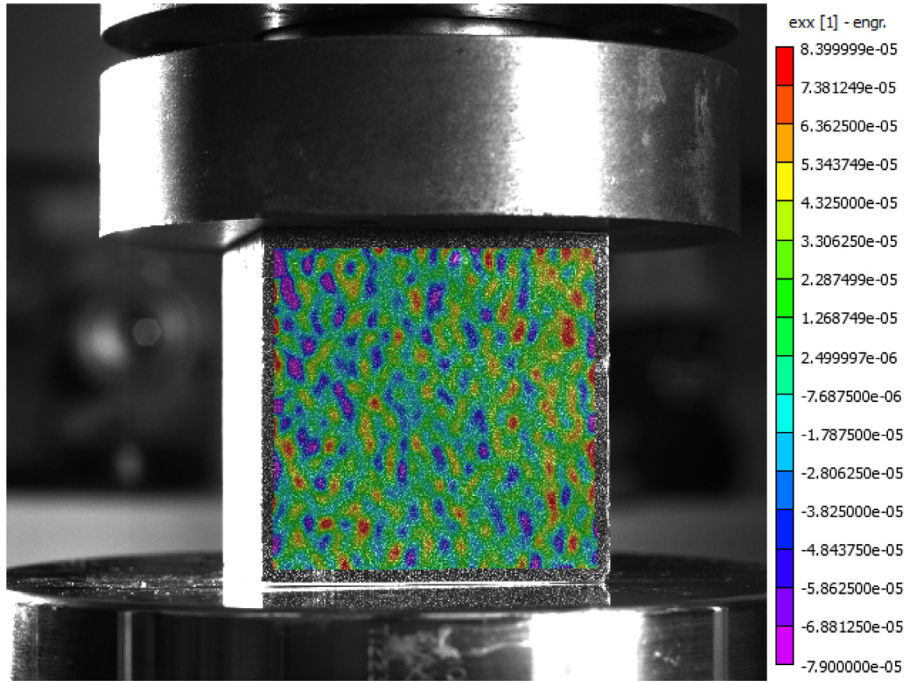


Fig. 3. Selected area for DIC strain field - Transverse strain (ϵ_{xx}).

where:

- $\mathbf{f}^T(\mathbf{x}) = \{f^{(1)}(\cdot), \dots, f^{(P)}(\cdot)\}$ consists of P arbitrary functions, known as regression functions;
- $\boldsymbol{\beta} = \{\beta^{(1)}, \dots, \beta^{(P)}\}$ are the P unknown regression coefficients;
- σ^2 represents the constant variance of the Gaussian Random Field (GRF);

$Z(\mathbf{x})$ consists of a GRF with 0 mean, unit-variance, and underlying correlation function $R(\mathbf{x}, \mathbf{x}'; \boldsymbol{\theta})$ that describes the correlation between two samples points and depends on the vector of hyperparameters, $\boldsymbol{\theta}$.

By definition, Gaussian processes are fully characterized by their mean vector $\mathbf{f}(\mathbf{x})^T \boldsymbol{\beta}$ and an autocovariance function $R(\mathbf{x}, \mathbf{x}'; \boldsymbol{\theta})$. Additionally, a corollary of this assumption is that every finite subset of realizations of such a field follows a multivariate Gaussian distribution. Consequently, denoting as $\mathcal{Y} = \{y^{(1)} = \mathcal{M}(\mathbf{x}^{(1)}), \dots, y^{(N)} = \mathcal{M}(\mathbf{x}^{(N)})\}$ the measured set containing N samples of a quantity of interest, their joint distribution reads:

$$\mathcal{Y} \sim \mathcal{N}_N(\mathbf{F}\boldsymbol{\beta}, \sigma^2 \mathbf{R}) \tag{2}$$

where:

- \mathbf{F} is the so-called design matrix. For the particular case of the so-called ordinary Kriging it reads:

$$F_{ij} = f_j(\mathbf{x}^{(i)}) = \mathbf{1}, i = 1, \dots, N; j = 0, \dots, P$$

- \mathbf{R} corresponds to the correlation matrix. It reads:

$$R_{ij} = R(\mathbf{x}^{(i)}, \mathbf{x}^{(j)}; \boldsymbol{\theta}), i, j = 1, \dots, N$$

In realistic scenarios, the parameters used to define the joint distribution Eq. (2) are unknown and must be estimated. Our goal in this paper is to deploy the methodology for training Kriging models to infer such parameters using the data obtained from DIC measurements. Once these parameters are known, it is possible to sample new paths of the Gaussian process. They will have similar properties to the measured data and can be used on the stochastic reconstruction of the quantity of interest. Ultimately, we focus on obtaining the autocovariance function, often called *kernel*, as this is the most important and overlooked step when sampling new paths.

Estimator of unknown parameters

Adopting a frequentist point of view, the unknown parameters are estimated from a two-level process. First, it is assumed that the correlation function $R(\mathbf{x}, \mathbf{x}'; \boldsymbol{\theta})$ is known. Under this assumption, we can compute \mathbf{R} and then evaluate $\hat{\boldsymbol{\beta}}$ and $\hat{\sigma}^2$ as shown in [26,27].

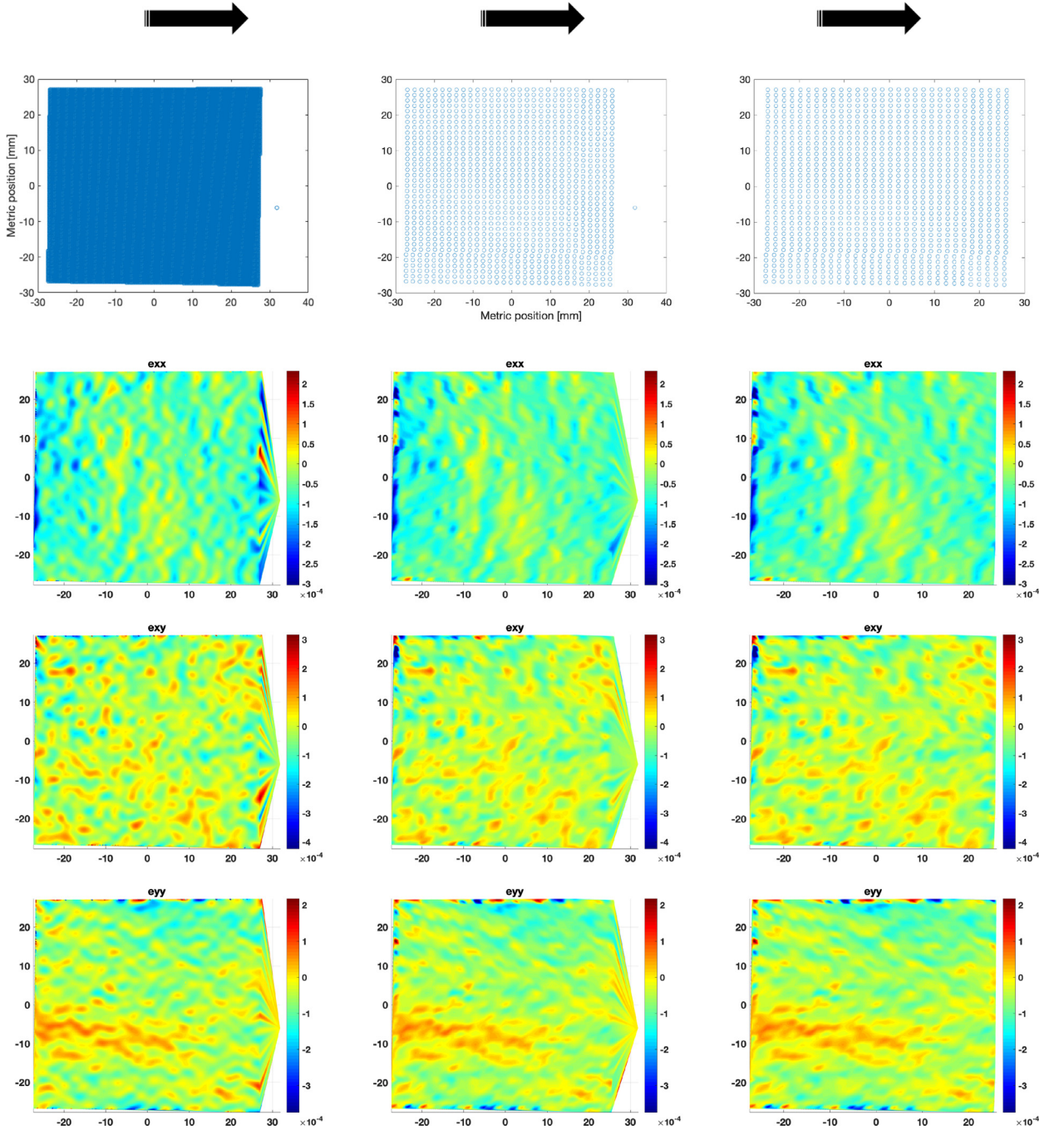


Fig. 4. Sample 21 (image 14) - data cleaning process: removal of duplicate data (first column) and outliers (second column). Final data is represented by the third column, for ϵ_{xx} , ϵ_{yy} , ϵ_{xy} strain fields.

$$\hat{\beta} = \hat{\beta}(\theta) = (\mathbf{F}^T \mathbf{R}(\theta)^{-1} \mathbf{F})^{-1} \mathbf{F}^T \mathbf{R}(\theta)^{-1} \mathbf{y}$$

$$\sigma^2 = \sigma^2(\theta) = \frac{1}{N} (\mathbf{y} - \mathbf{F} \hat{\beta})^T \mathbf{R}(\theta)^{-1} (\mathbf{y} - \mathbf{F} \hat{\beta}) \quad (3)$$

The correlation function, however, is rarely known beforehand. For this reason, the second step corresponds to estimating the kernel and its parameters. Instead of deriving an *ad hoc* correlation function, in practice, one finds the best θ for a set of well-known

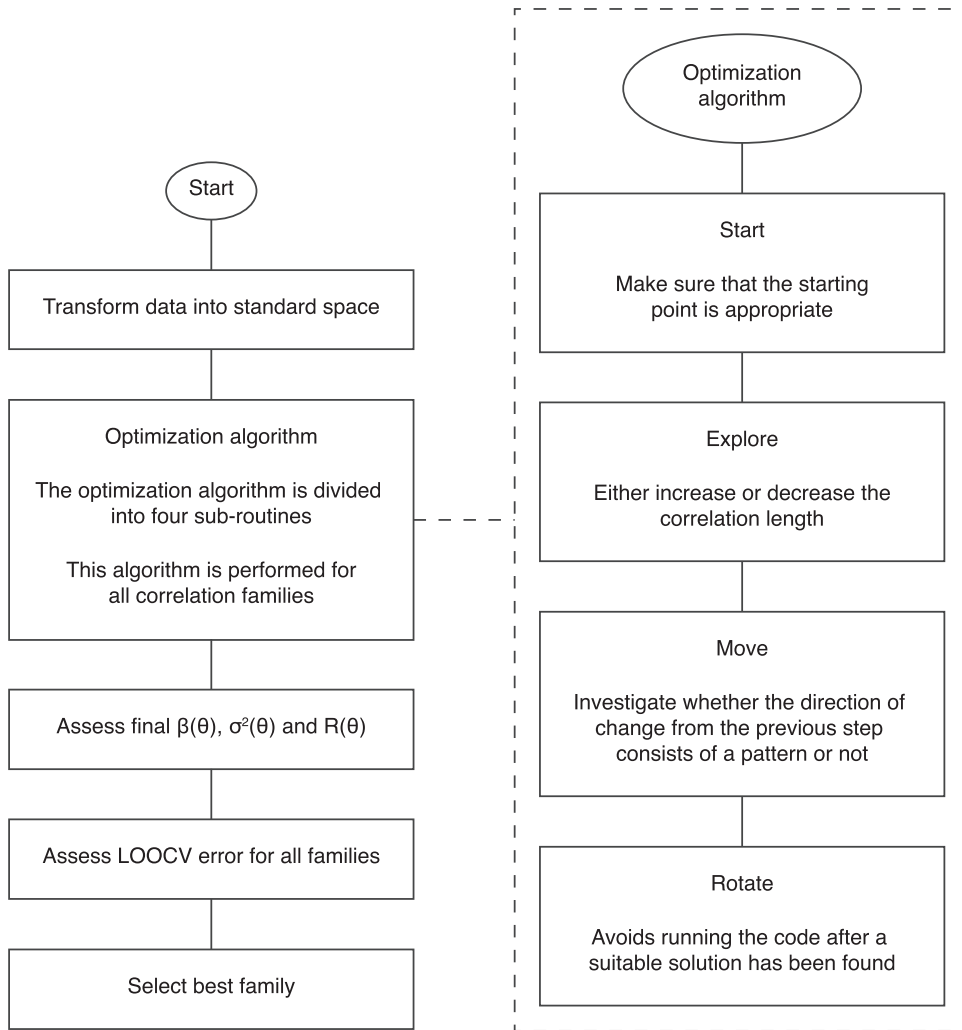


Fig. 5. Algorithm’s main process.

correlation families. Afterwards, the best combination of θ and correlation family is selected. Hence, the problem becomes similar to an inference problem.

A common inference technique for computer experiments is the maximum likelihood estimation (MLE). According to this method, the best set of parameters is the one which maximizes the likelihood function. In practice, however, we minimize the log of the likelihood function, as described in Eq. (4). Such an optimization problem is not trivial to solve [28]. It is not convex, and its objective function is expensive to evaluate, as it requires the determinant and the inverse of the correlation matrix. To solve such a global optimization problem efficiently, the authors implemented the algorithm developed by Lophaven et al. [29], widely applied in the Kriging methodology [29,30].

$$\hat{\theta} = \arg \min_{\theta} \frac{1}{2} [\log(\det \mathbf{R}) + N \log(2\pi\sigma^2) + N] \tag{4}$$

As the correlation family is unknown, the authors optimized the parameters for all the correlation families presented in Table 1. After optimizing the parameters for all families, it was still necessary to rank them, which was done according to their mean squared error (MSE), estimated via leave-one-out cross-validation (LOOCV) [27]. The rationale of LOOCV is the following: at each iteration, one input data is used as a validation set, whereas the remainder data trains the Kriging model. After repeating this process for each point of the training set, it is possible to estimate the MSE. Finally, Fig. 5 summarizes the framework for inferring the kernel that best describes the collected data.

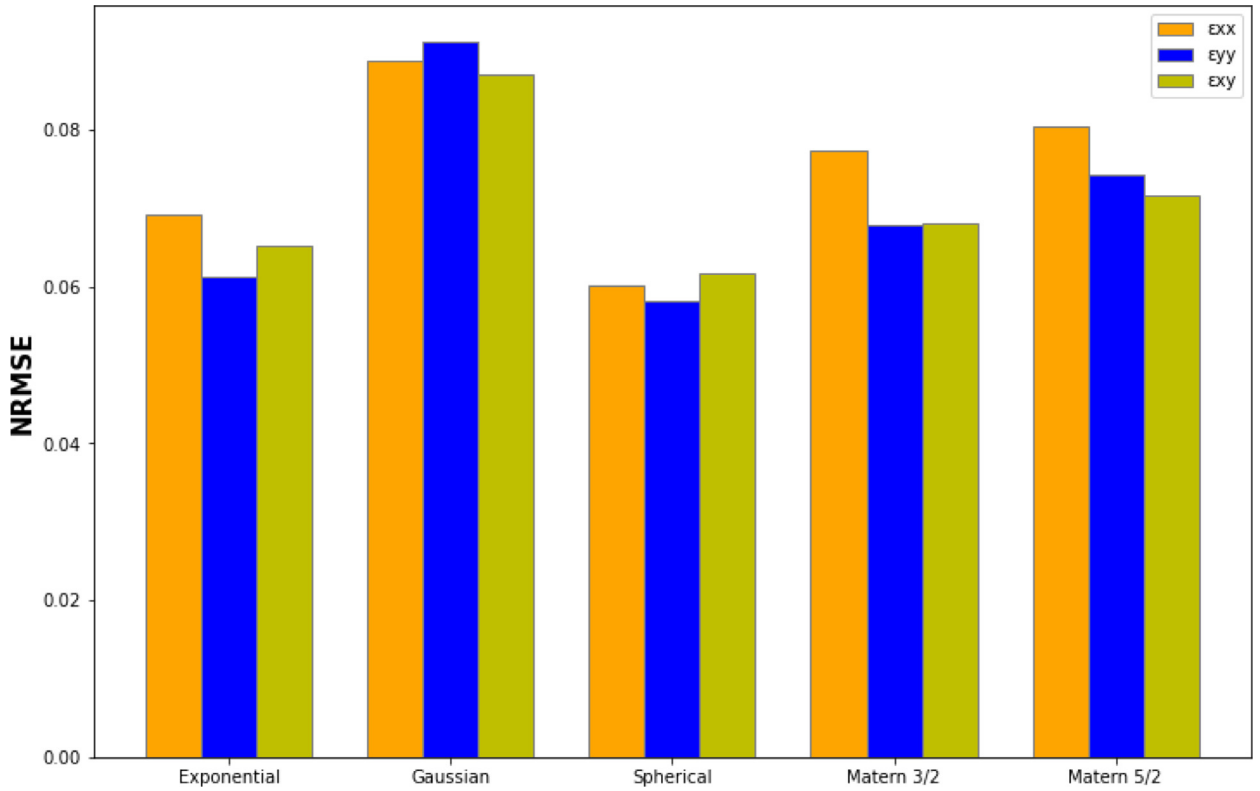


Fig. 6. Metamodeling normalized error for ϵ_{xx} , ϵ_{yy} and ϵ_{xy} strains and all correlation families for Sample 21.

Table 1
Correlation families evaluated at the algorithm.

Family	Function	Reference
Gaussian	$R(x, x'; \theta) = \exp\left(-\left(\frac{x-x'}{\theta}\right)^2\right)$	[31]
Exponential	$R(x, x'; \theta) = \exp\left(-\left(\frac{ x-x' }{\theta}\right)\right)$	[31]
Spherical	$R(x, x'; \theta) = 1 - 1.5\xi + 0.5\xi^3$, s.t., $\xi(x, x', \theta) = \min\left(1, \frac{ x-x' }{\theta}\right)$	[29]
Matern	$R(x, x'; \theta, \nu = \frac{3}{2}) = \left(1 + \frac{\sqrt{3} x-x' }{\theta}\right) \exp\left(-\frac{\sqrt{3} x-x' }{\theta}\right)$	[25]
Matern	$R(x, x'; \theta, \nu = \frac{5}{2}) = \left(1 + \frac{\sqrt{5} x-x' }{\theta} + \frac{\sqrt{5}(x-x')^2}{2\theta^2}\right) \exp\left(-\frac{\sqrt{5} x-x' }{\theta}\right)$	[25]

Table 2
Correlation functions ranking - Sample 21.

	$\theta_{\epsilon_{xx},x}$	$\theta_{\epsilon_{xx},y}$	$\text{NRMSE}_{\epsilon_{xx}}$	$\theta_{\epsilon_{yy},x}$	$\theta_{\epsilon_{yy},y}$	$\text{NRMSE}_{\epsilon_{yy}}$	$\theta_{\epsilon_{xy},x}$	$\theta_{\epsilon_{xy},y}$	$\text{NRMSE}_{\epsilon_{xy}}$
Exponential	0.025000	0.20000	0.069109	0.057017	0.014785	0.061239	0.024489	0.030433	0.065320
Gaussian	0.050000	0.05000	0.088935	0.050000	0.050000	0.091345	0.050000	0.050000	0.087095
Spherical	0.034306	0.14248	0.060205	0.092498	0.052369	0.058183	0.060010	0.066190	0.061712
Matern ($\nu = 3/2$)	0.050000	0.05000	0.077357	0.050000	0.050000	0.067904	0.050000	0.050000	0.068057
Matern ($\nu = 5/2$)	0.050000	0.05000	0.080511	0.050000	0.050000	0.074179	0.050000	0.050000	0.071636

Method validation

Rock’s DIC strain correlation function

Taking Sample 21 as a reference, Table B.1 depicts the calculated hyperparameters obtained from the displacement fields measured by the DIC technique at 10kN. The normalized cross-validation error for each kernel family is also summarized in Fig. 6. The authors chose to assess the hyperparameters at these peaks because all samples were in the elastic state under this load, as depicted in Fig. A.7 in Appendix A. The algorithm results for all samples are available in Appendix B.

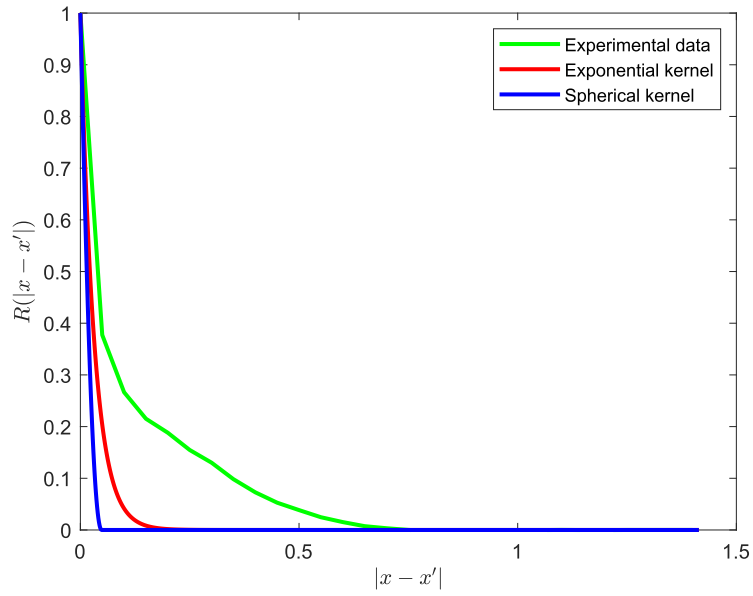


Fig. 7. Comparison between correlation estimated directly from data (green) and the ones obtained with Exponential (red) and Spherical (blue) kernels. (For interpretation of the references to color in this figure legend, the reader is referred to the web version of this article.)

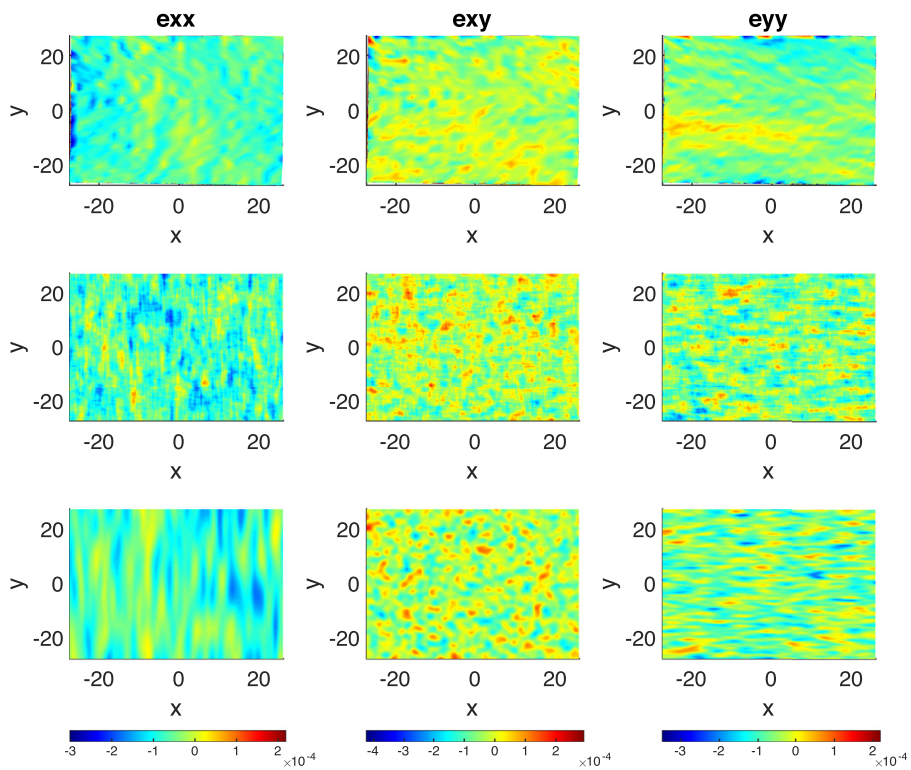


Fig. 8. Fields obtained from data (first row), Spherical kernel (second row) and Exponential kernel (third row) for Sample 21. From left to right: ϵ_{xx} , ϵ_{xy} , ϵ_{yy} .

One can note that, for this sample, the spherical kernel presents the best convergence rate. Nonetheless, the rates for all families are quite similar, which leads to no clear better correlation families for the present case. Although this conclusion relies on the accuracy of the calculated hyper-parameters. Such results allows the usage of different correlation families for Gaussian regression of strain fields, as long as the hyperparameters are respected.

Stochastic reconstruction from DIC data and algorithm output

The stochastic reconstruction of the strain field from experiment and DIC data, are characterized by the data marginal distribution and second moment properties in this study. The covariance measurement is based on the separation distance between each pair of elements in a numerical analysis, which is also defined by the covariance functions selected by the algorithm.

Figure 7 shows a comparison between the autocorrelation function estimated by the experimental data obtained for Sample 21 and the ones considering the Spherical Exponential covariance functions. Note that because the optimization is performed in a scaled space, the x-axis is depicted as scaled. Additionally, Fig. 8 depicts the surfaces obtained using the estimated kernels.

Conclusion

The primary contribution of this paper is introducing a method for stochastic image reconstruction of material properties, primarily based on the methodology for training Gaussian processes. The proposed method is versatile and straightforward, solely relying on the assumption that a Gaussian random field can accurately represent the quantity of interest. Assuming this premise holds, it is possible to characterize the kernel that best represents any physical property of the material. For tuning the kernel and its parameters, only a set of measures of the quantity of interest is needed. Once the kernel is known, it is possible to sample as many Gaussian random fields as needed to analyze the problem.

We showcase our methodology employing a case study of compressed limestone rocks. Based on the strain data collected with digital image correlation, we show the steps needed to obtain the kernel that best represents the data. Additionally, we show the fields that can be obtained with the estimated kernels. Specifically to this case study, we conclude that although spherical and exponential families often lead to the best results, no clear best representation of the correlation family can be asserted. Indeed, our results show that the correlation families perform similarly once their parameters are optimized.

Declaration of Competing Interest

The authors declare that they have no known competing financial interests or personal relationships that could have appeared to influence the work reported in this paper.

Data availability

Data will be made available on request.

Acknowledgments

The authors thank Dr. David Jesson and the University of Surrey for supporting the experiments, as well as the Santander Mobility Award for funding the experimental process of this work. This study was financed in part by the Coordenação de Aperfeiçoamento de Pessoal de Nível Superior - Brasil (CAPES) - Finance Code 001.

Appendix A

DIC system preparation and results

Speckle pattern

A random speckle pattern needs to be applied to sample's surface in order to guarantee DIC's measurements, since the basic operation of DIC is tracking a pattern in a sequence of images. According to Sutton et al. [15], an ideal surface texture should be isotropic, with no preferred orientation.

There are different ways to create/apply a speckle pattern into the object surface. For this work, the process described in Fig. A.1 of [32] was used, whereby the speckle diameter was based on the experimental area of interest of the specimen, resulting in a known pixel per millimeter for the image and allowing optimal speckle sized based on a requirement of 7 pixels per speckle with 50% of the area covered by speckles. Following this process, the speckle was generated using Correlated Solutions' SpeckleGen 1.0.5 with the following parameters:

- Speckle diameter: 0.111 mm;
- Density: 70%;
- Variation: 95%.

The pattern was printed in tattoo paper and then, with a damp cotton, the pattern was attached to the specimen's surface. Figure A.1 depicts a sample with the pattern on its surface.

Setting Up of Camera system

Once the sample was fixed on the test machine, the cameras and lights were also placed and adjusted. The cameras were positioned from a distance of 410 mm from samples, making sure the field of view covered the specimen's entire surface. The tests involved 2D-DIC and Stereo-DIC analysis. The first 3 tests were carried out with 2D-DIC to calibrate the system and define maximum load. The 2D-DIC consists in one camera, and assumes planar test piece, in which any out-of-plane motion cause errors in analysis. Stereo-DIC in the other hand, has two cameras placed in front of the specimen, which was used in all analysis except for calibration analysis. The stereo-DIC analysis were carried out on both front (System 1) and back (System 2) surfaces of each sample, as can be seen in Fig. A.2. The light sources were positioned sideways to prevent reflection by the specimen from saturating the cameras. The VIC-Snap software, with the cameras images on, presents the regions that are affected by light reflection with a red color, in a way that it is possible to adjust the light position and intensity until no or little reflection is seen on specimen surface. Figure A.3 presents the light reflection/adjustment on all 4 cameras of both Systems 1 and 2.

Calibration

For this work, 50 pictures were taken with the calibration board held at various angles and locations, Fig. A.4 presents a few examples of the calibration board made for the experiments.

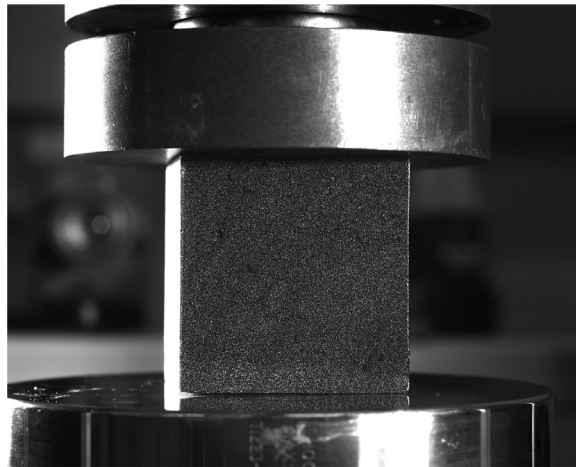


Fig. A.1. Speckle pattern over sample surface.

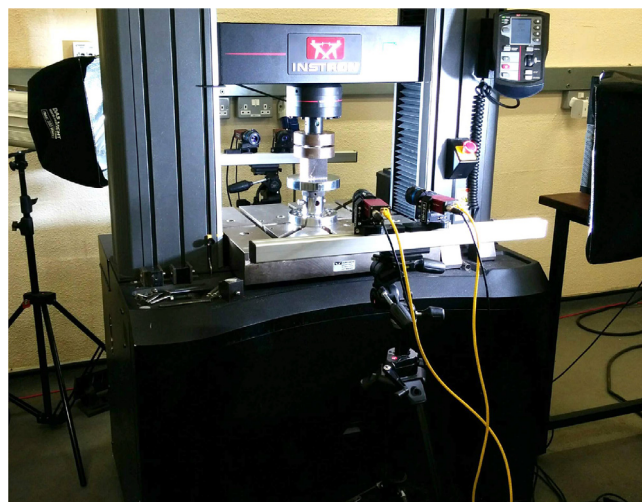


Fig. A.2. Experiment apparatus.

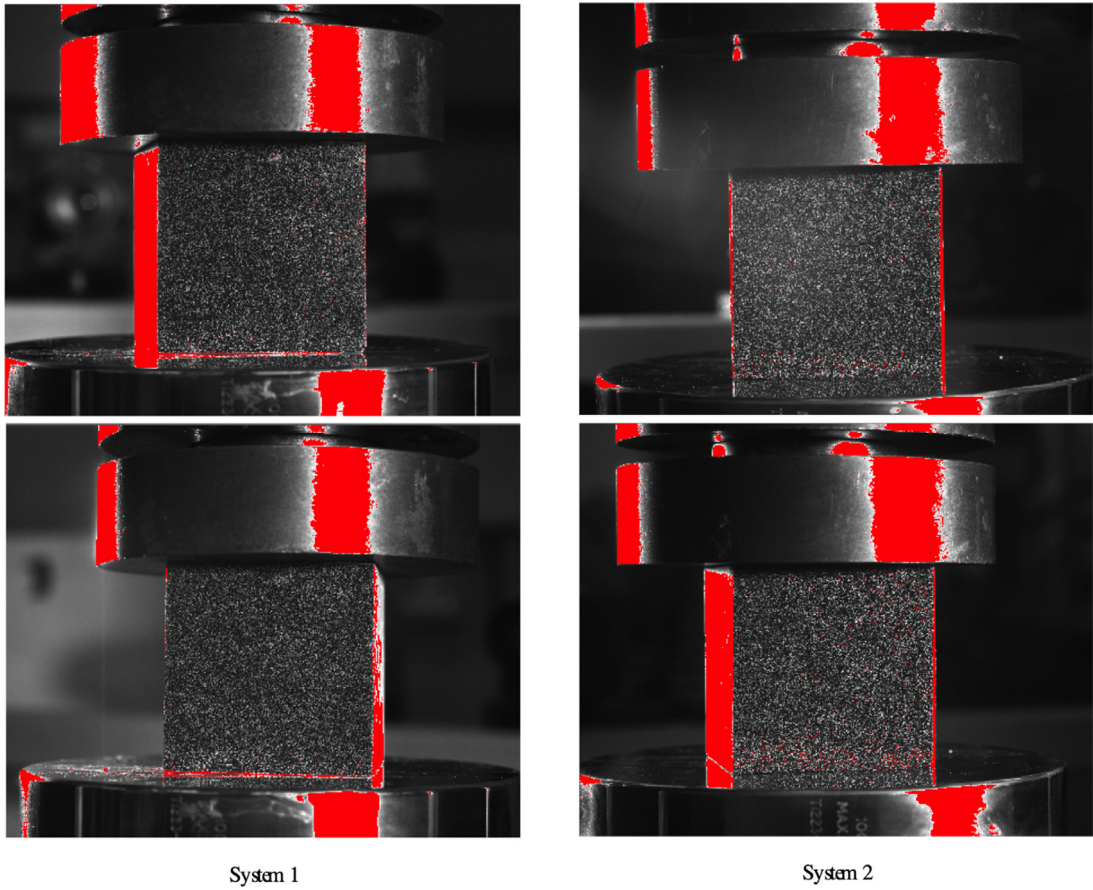


Fig. A.3. Light adjustment: System 1 (front cameras) and System 2 (back cameras).

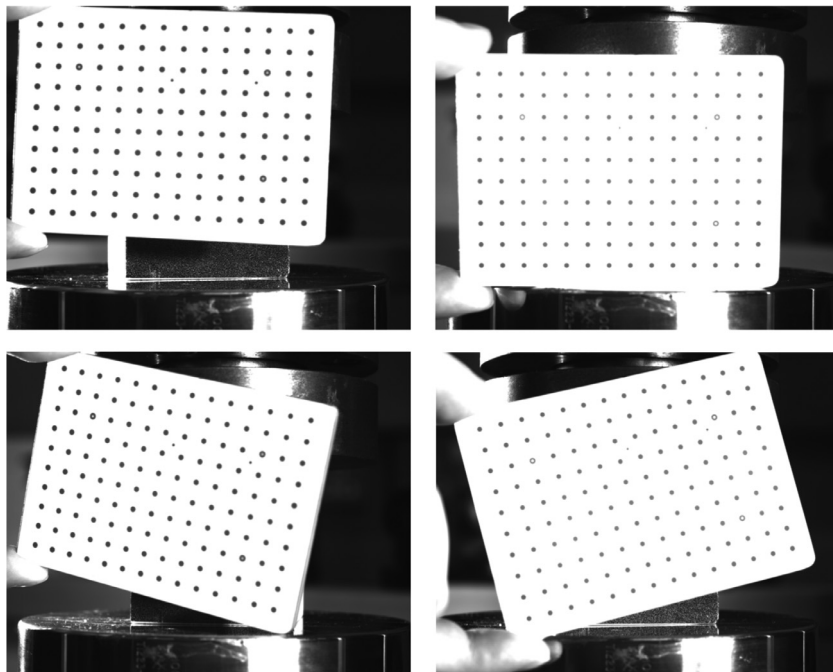


Fig. A.4. Calibration images examples.

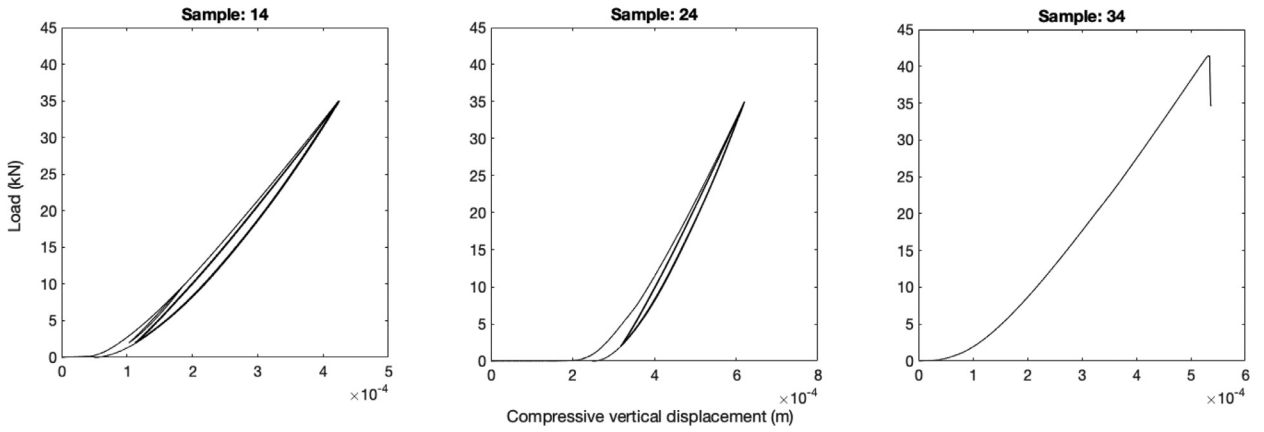


Fig. A.5. Cyclic loading tests on samples: 14, 24 and 34.

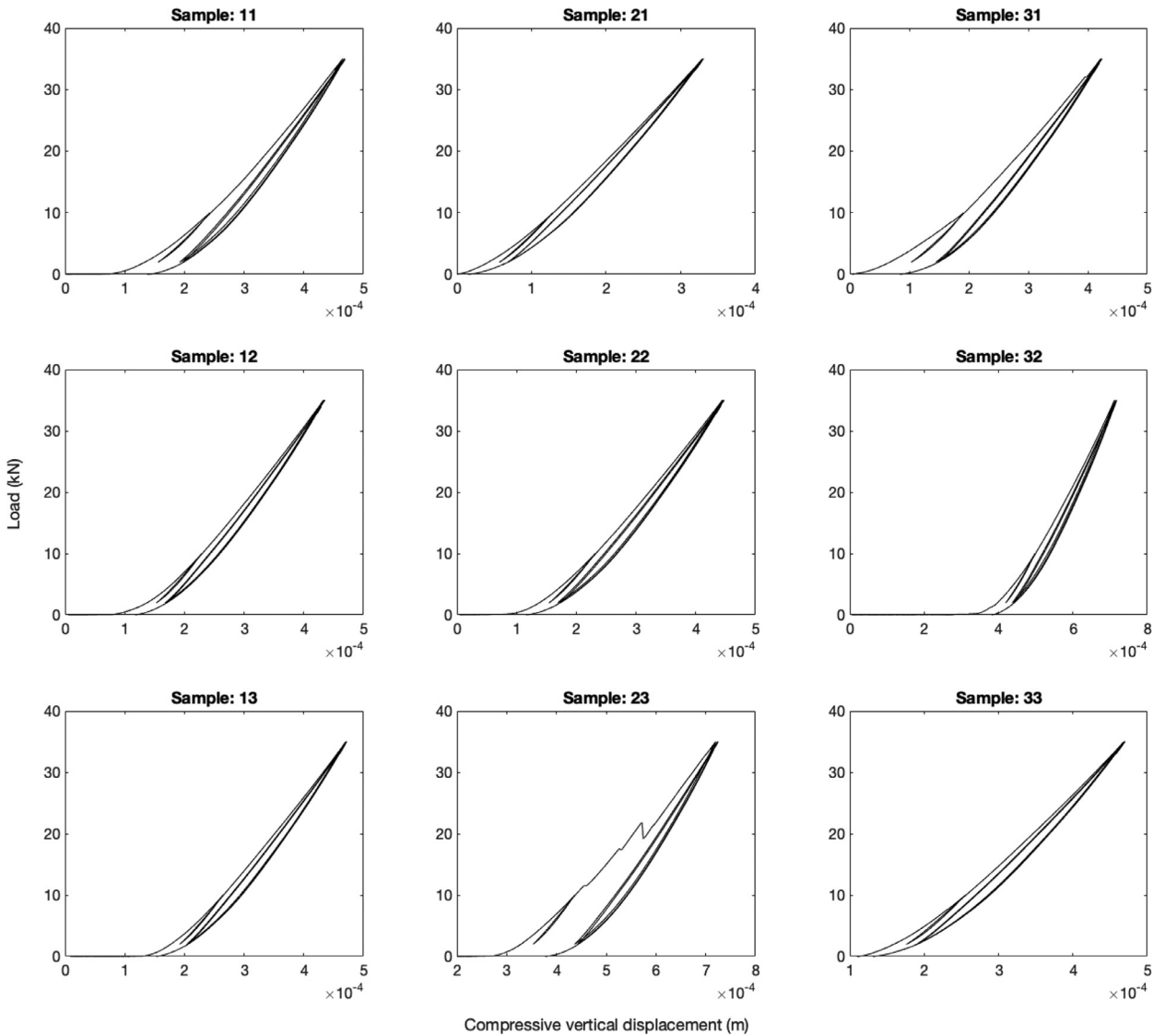


Fig. A.6. Samples cyclic loading x displacement.

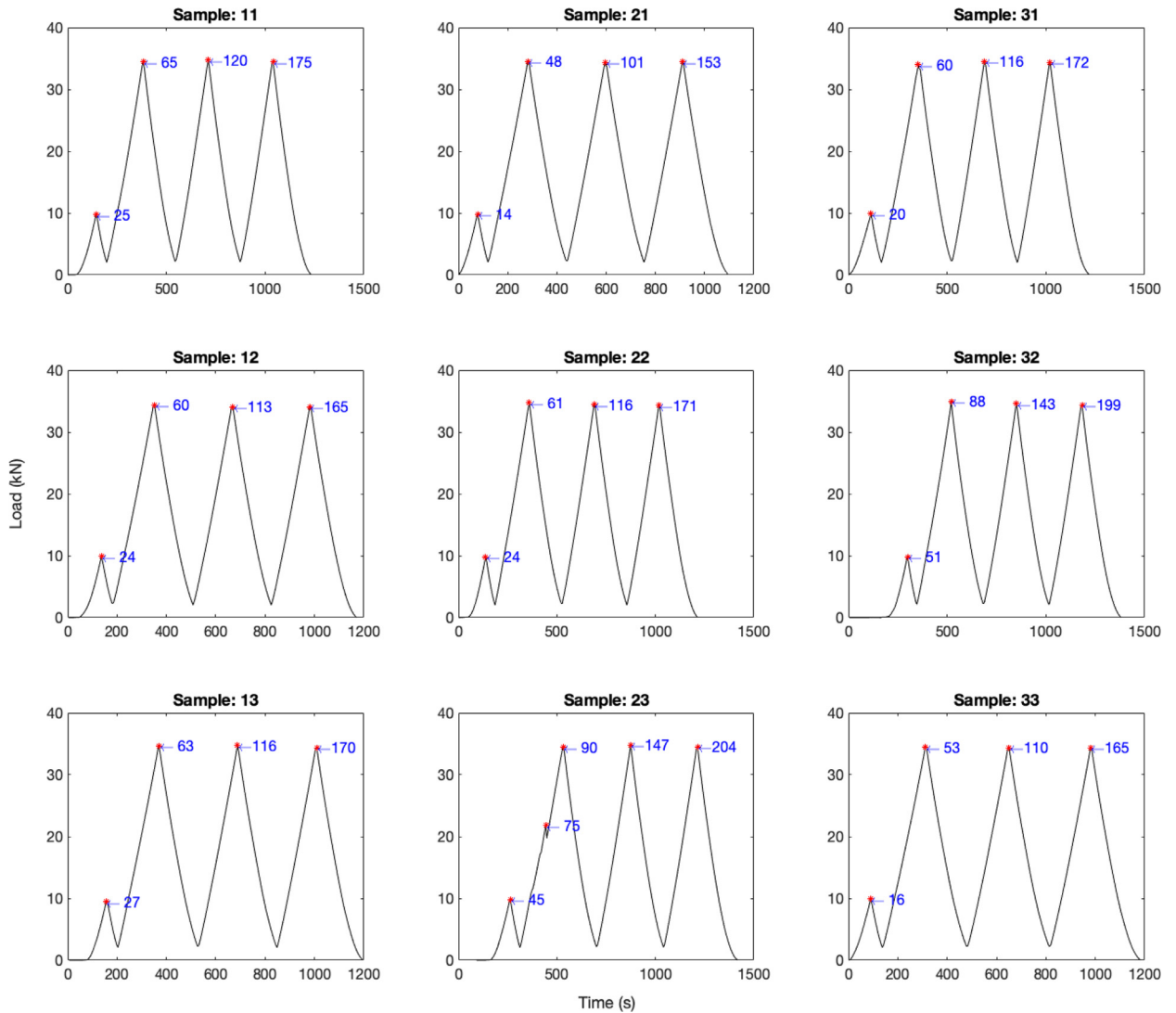


Fig. A.7. Samples cyclic loading x time. The highlighted points identifies the picture number of the peaks.

The score at VIC-3D should be below 0.05, ideally, below 0.03, to ensure a calibrated stereo system. For the present work, a score of 0.006 was acquired.

The software was preset in order to take one picture in each camera in every 6 seconds. Each analysis, besides the one used to calibrate, has around 200 pictures from each System.

Images post-processing

After collecting images during test using VIC Snap, the following steps should be done for image processing:

1. In the VIC-3D, open speckle images
2. Create polygon in the image. The selected polygon for all images in this work, is a square covering all specimen surface.
3. Choose subset size. The software recommends it to be between 49 and 53. Subset of 51 was assumed in this work.
4. Choose set size (between 1/4 and 1/3 of the subset size). In the present work, the steps number was firstly 15, but as were noted some differences in deformation field, the steps of 7 was later adopted and the images were re-processed considering this step number. (It is in the literature that the steps can be 1/3 of the subset size, which implies that a step number lower than that would not present difference in the DIC analysis. However, the rock presented a significant change according to steps number). Thus, the present study considered in all analyzed samples the set size of 7 steps.
5. Create start point and wait until 100%

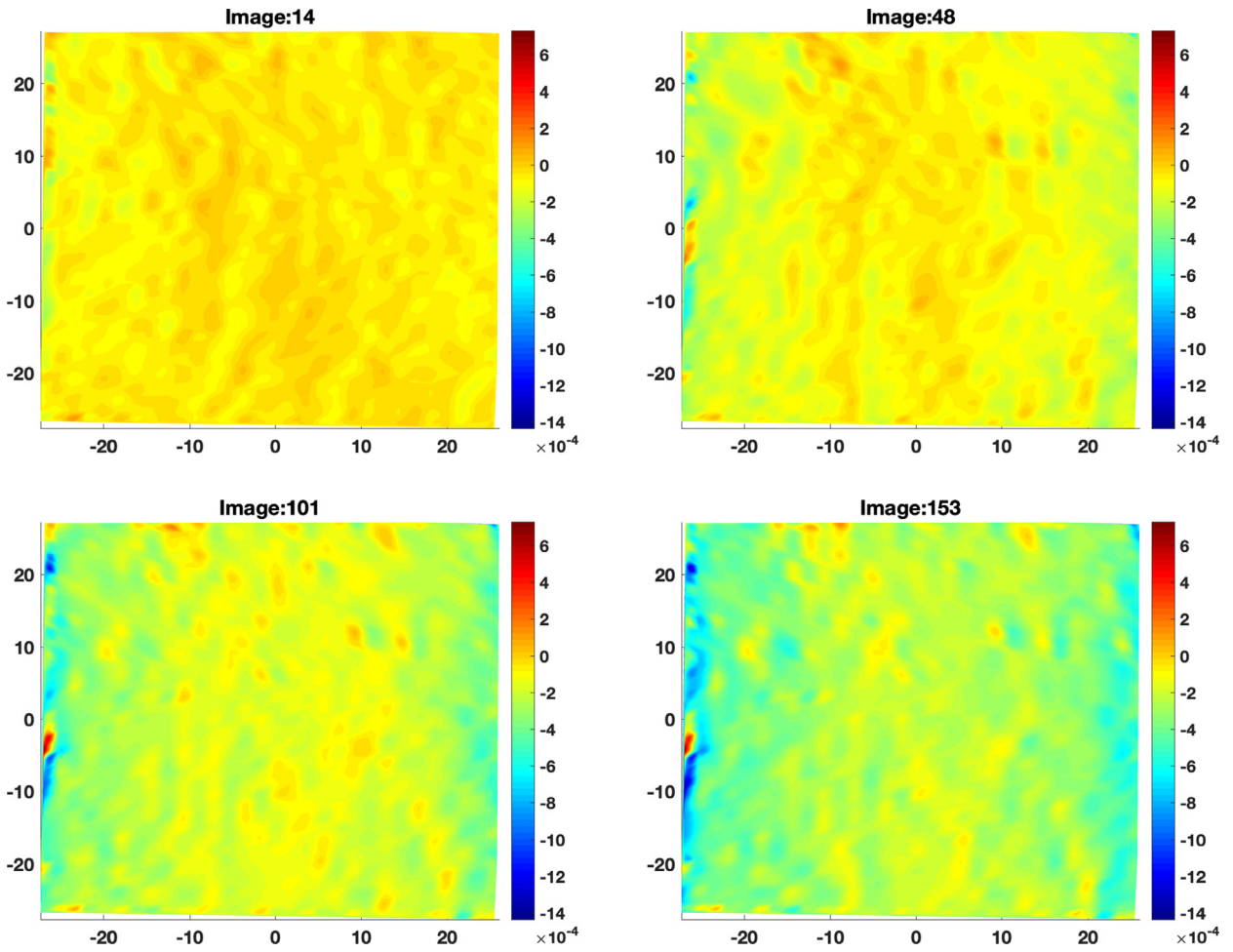


Fig. A.8. ϵ_{xx} strain of Sample 21, Images: 14, 48, 101, and 153. System 1 (front cameras).

6. Run
7. Calculate strain, wait for 100%
8. Visualize results and select desired strain.

The filter size chosen in this work was 11.

Loading design

Three samples were used to calibrate the loading system machine. As the rock’s compressive and shear strength were not known, it was necessary to calibrate at what was the maximum load before specimen failure. Samples 14, 24, and 34, used to calibrate the load system, have their load x compressive displacement behavior plotted in Fig. A.5.

Sample 34 was the first one to be tested. The goal of this test was applying axial load until rock failure, which was reached in approximately 43 kN. Once aware of the maximum load, the next step was defining a cyclic load, in a way that it could be possible to evaluate strains in a same load but multiple times. Sample 24 was tested with 3 cycles: load until 35 kN, unload to 2 kN, load until 35 kN, unload until 2 kN, load until 35 kN and unload until 0 kN.

In order to be conservative and avoid plastic deformation, a new cyclic load was designed with Sample 14. A lower first peak load was set, and followed the same 3 cycles as Sample 24: load until 10 kN, unload until 2 kN, load until 35 kN, unload to 2 kN, load until 35 kN, unload until 2 kN, load until 35 kN and unload until 0 kN.

All samples cyclic loading x displacement are depicted in Fig. A.6. For all those tests were assumed a first peak of 10 kN in the first cycle, as previously described in the calibration with sample 14. Higher dispersion in Samples 11 and 31 may indicate plastic deformation after first and second cycle. Sample 23 failed during the test under 23 kN load approximately. Sample 22 was accidentally

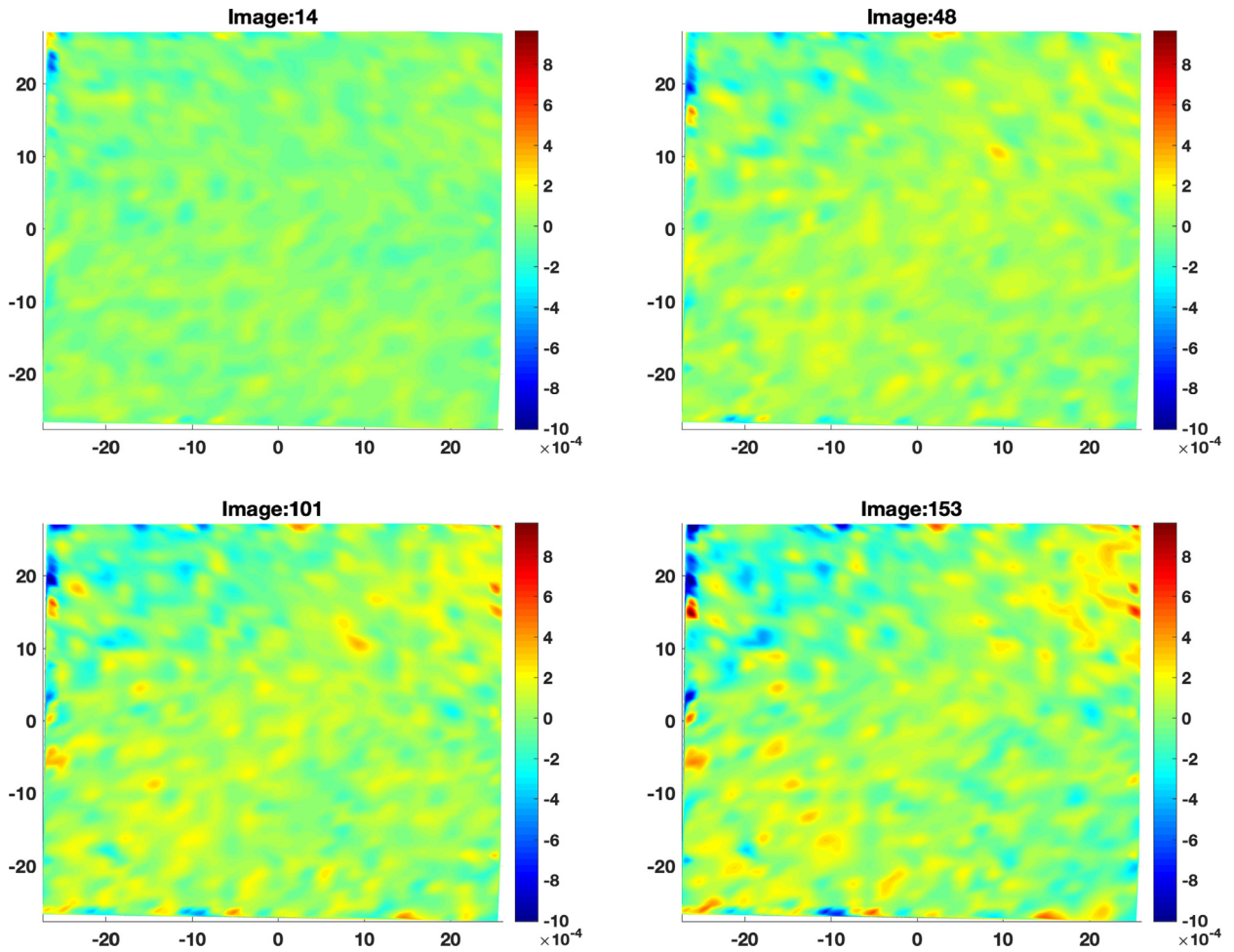


Fig. A.9. ϵ_{xy} strain of Sample 21, Images: 14, 48, 101, and 153. System 1 (front cameras).

broke before experiment, however, it still presented a similar behavior, even with a fracture on front surface. Sample 32 presented higher displacement when compared to other specimens.

The cameras were set to take one picture every 6 s, starting at the same time as the load machine. Thus, it is useful to track the image number according to the applied load in a specific moment. Figure A.7 shows the load x time of the tested samples, and indicates in red star the peaks of each experiment. The blue numbers refer to the DIC image number in each peak.

Strain field by peaks

Following the image number for test peaks, as plotted in Fig. A.7, the engineering strains for Sample 21, which presented a regular behavior, is presented in Figs. A.8, A.9 and A.10. One can note that even though images 48, 101 and 153 have the same load, the field strains are different. This observation may represent plastic deformation on sample, or not enough time for the specimen to return to its initial state after unloading.

Sample 23, the one that failed during the test, had also its strains plotted in Figs. A.11, A.12 and A.13. The fracture initiation can be clearly seen from image 75, at the moment the sample fails. However, ϵ_{xy} strain presents some tendency behavior from image 45 in advance, with 10 kN peak.

Sample 22 was already fractured before test, its strains peaks are depicted in Figs. A.14, A.15 and A.16. As expected, fracture is observed since the first peak in image 24, for all strains.

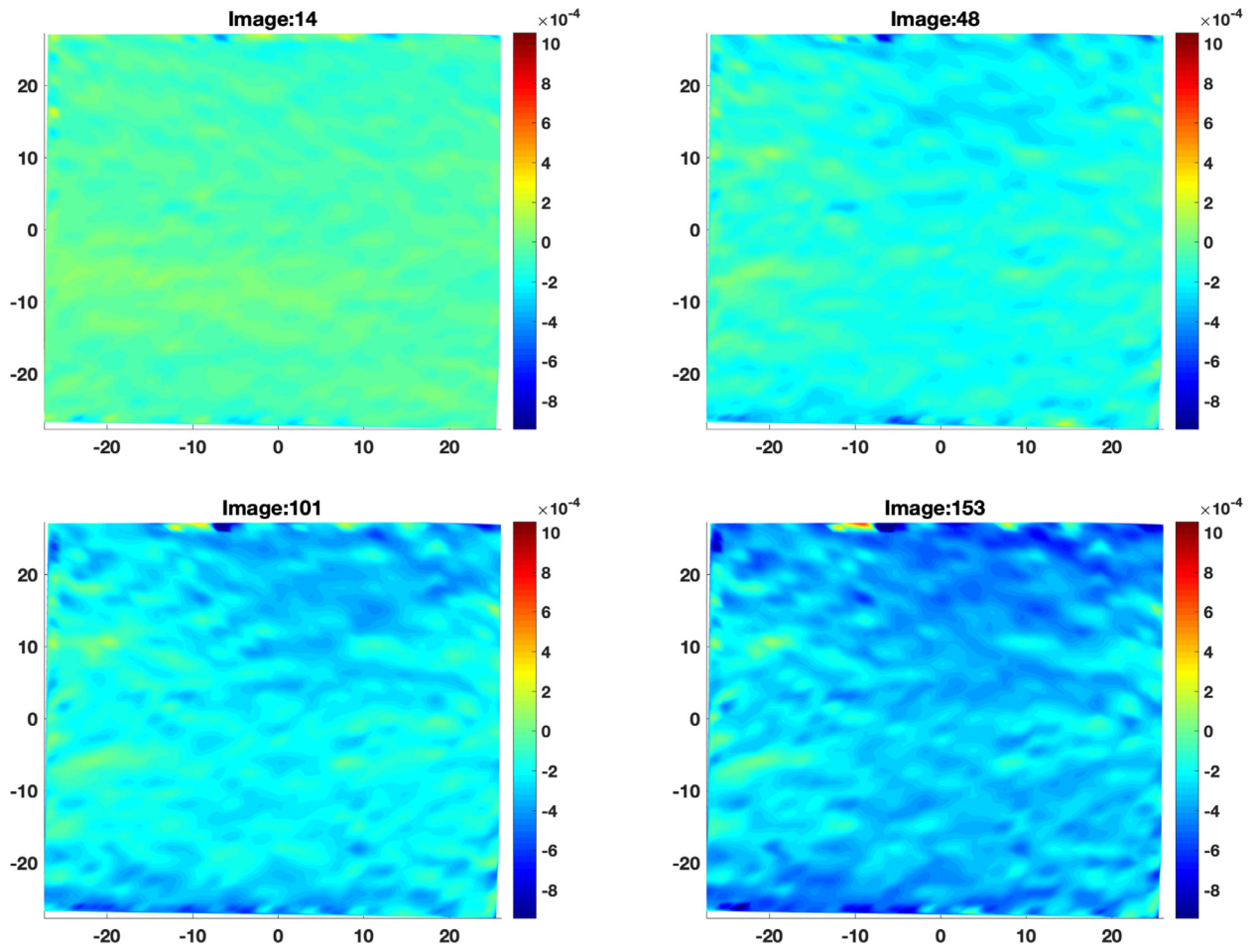


Fig. A.10. ϵ_{yy} strain of Sample 21, Images: 14, 48, 101, and 153. System 1 (front cameras).

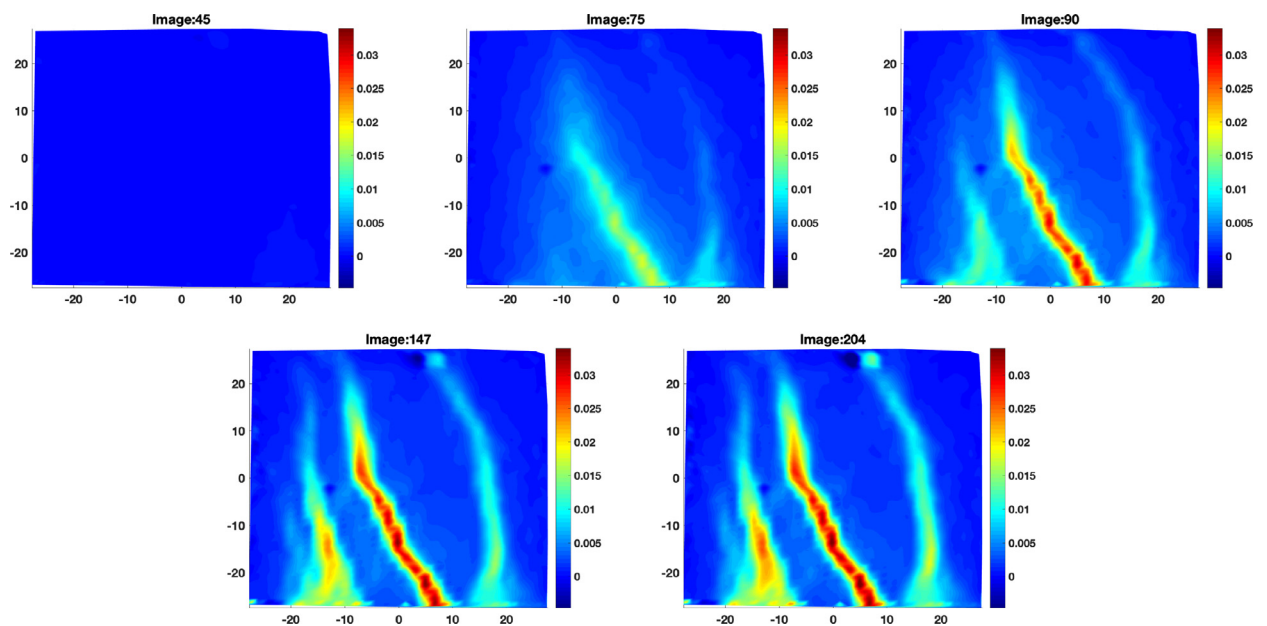


Fig. A.11. ϵ_{xx} strain of Sample 23, Images: 45, 75, 90, 147, and 204. System 1 (front cameras).

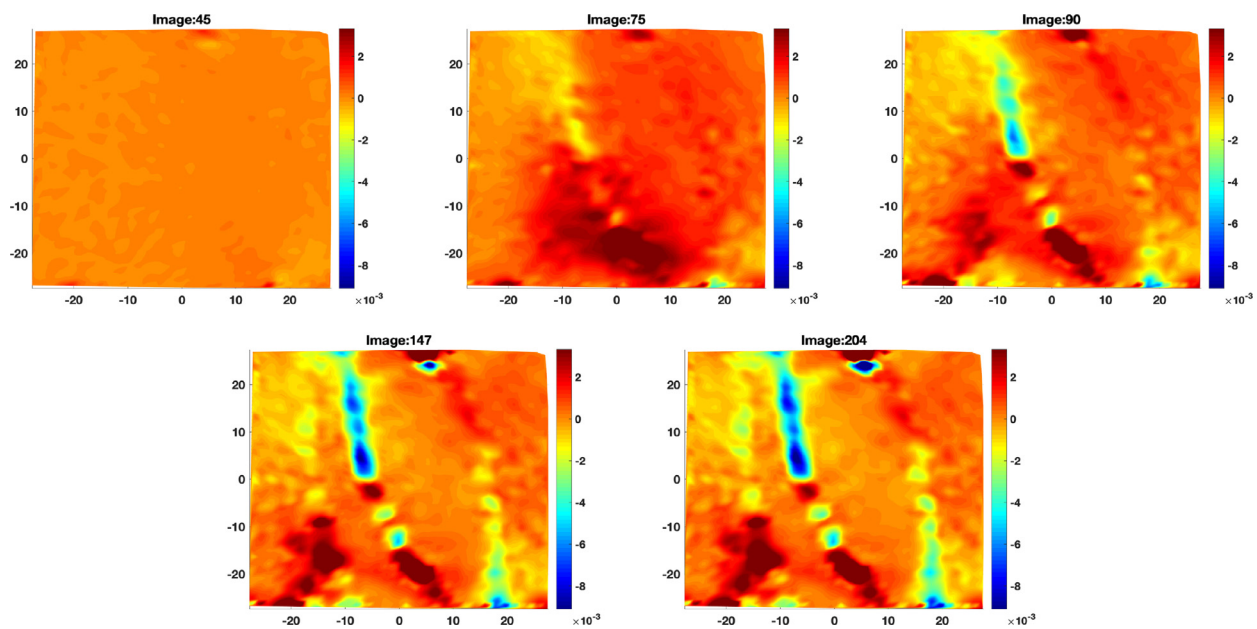


Fig. A.12. ϵ_{xy} strain of Sample 23, Images: 45, 75, 90, 147, and 204. System 1 (front cameras).

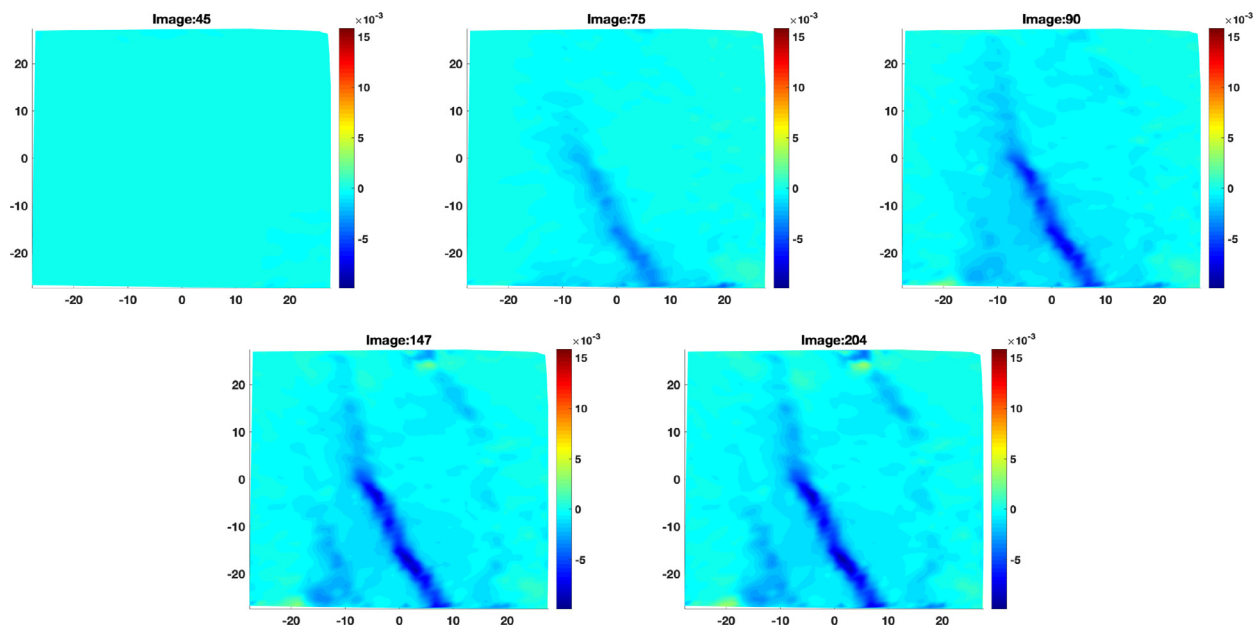


Fig. A.13. ϵ_{yy} strain of Sample 23, Images: 45, 75, 90, 147, and 204. System 1 (front cameras).

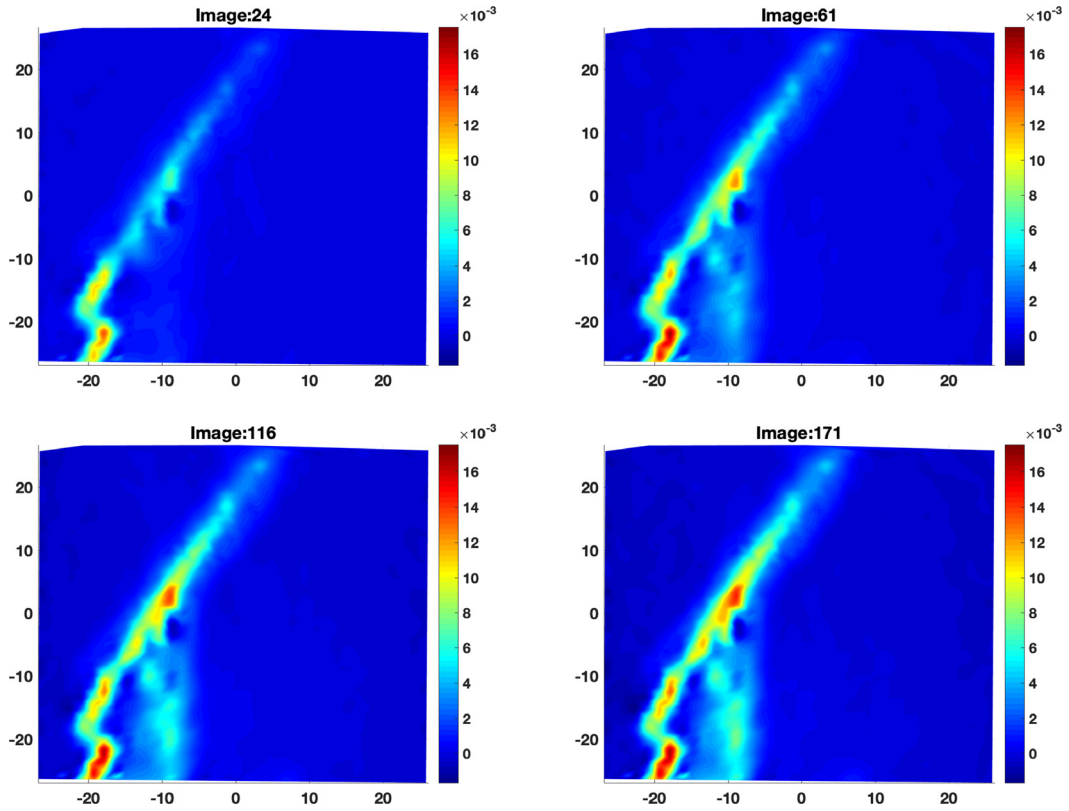


Fig. A.14. ϵ_{xx} strain of Sample 22, Images: 24, 61, 116, 171. System 1 (front cameras).

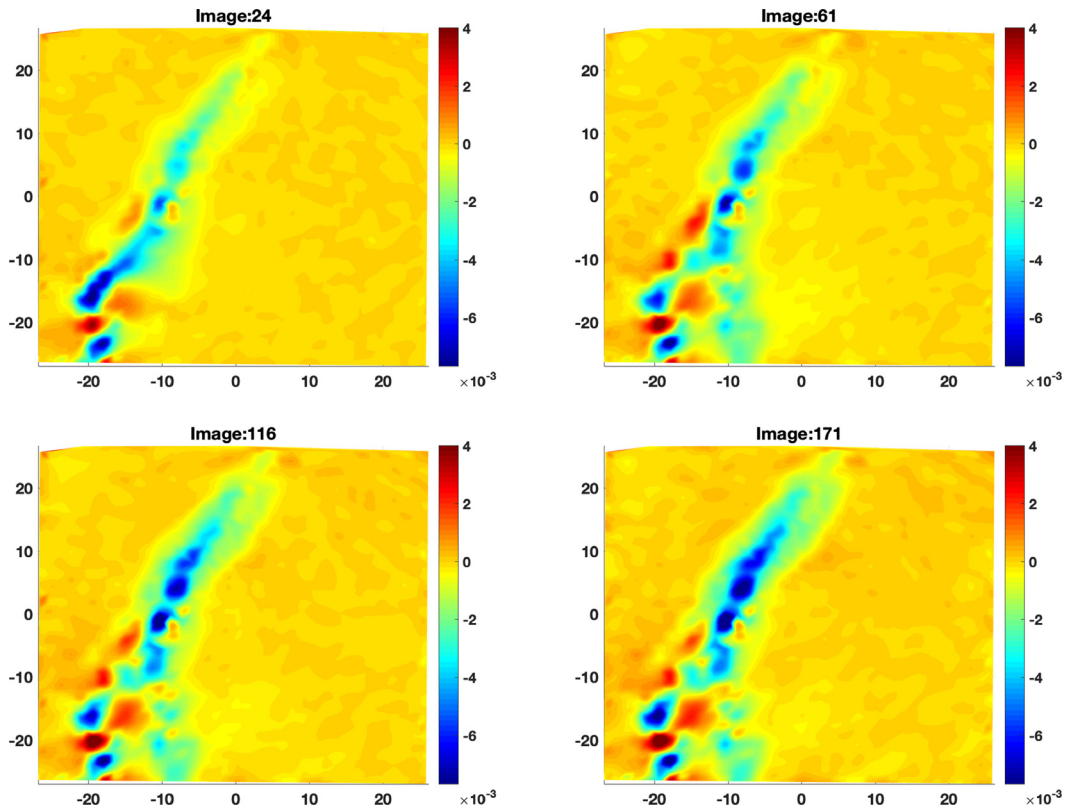


Fig. A.15. ϵ_{xy} strain of Sample 22 Images: 24, 61, 116, 171. System 1 (front cameras).

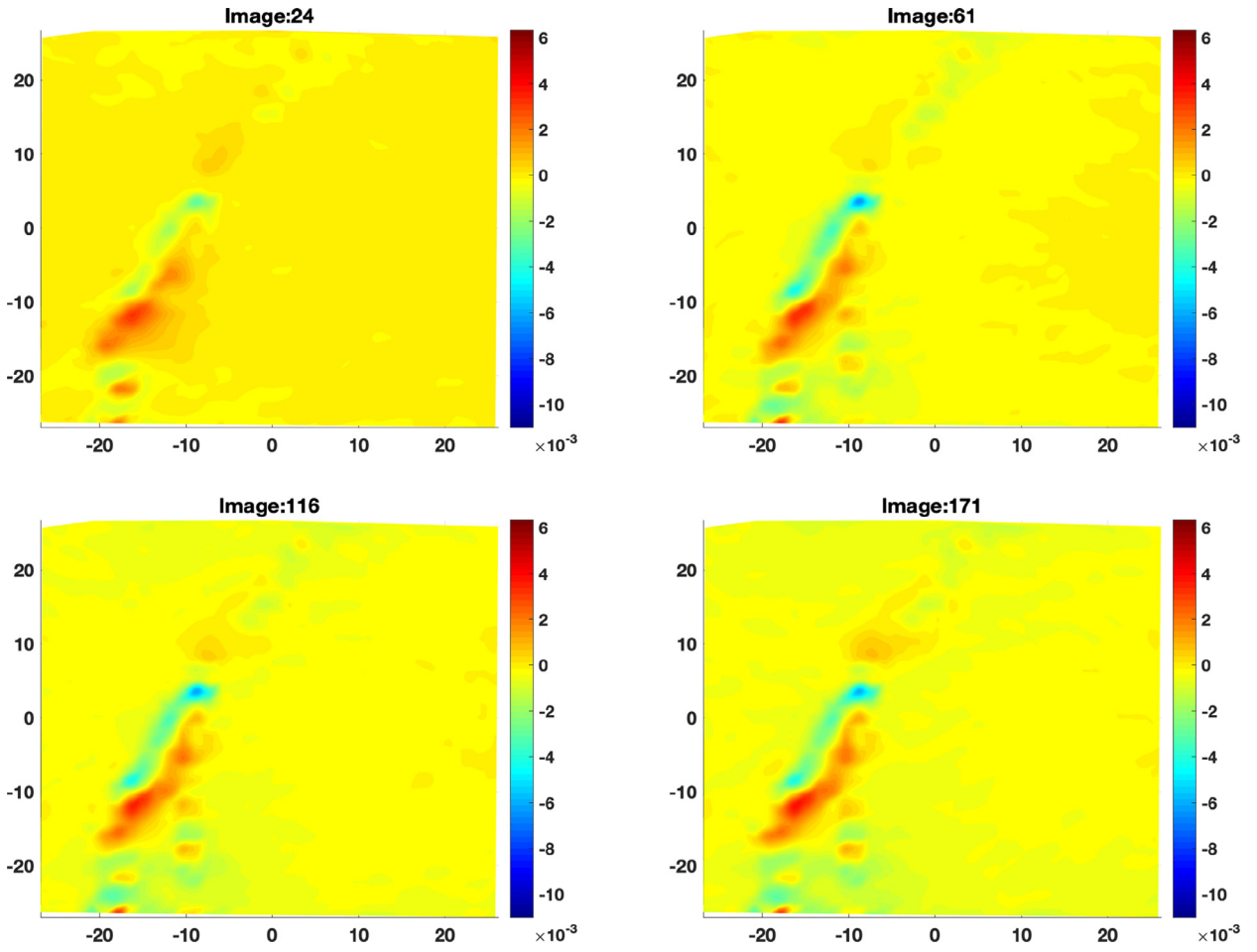


Fig. A.16. ϵ_{yy} strain of Sample 22, Images: 24, 61, 116, 171. System 1 (front cameras).

Appendix B

Tables B.1–B.9 present the algorithm results for all samples evaluated in the present study.

Table B.1
Algorithm results - Sample 11.

	$\theta\epsilon_{xx}x$	$\theta\epsilon_{xx}y$	$\text{NRMSE}\epsilon_{xx}$	$\theta\epsilon_{yy}x$	$\theta\epsilon_{yy}y$	$\text{NRMSE}\epsilon_{yy}$	$\theta\epsilon_{xy}x$	$\theta\epsilon_{xy}y$	$\text{NRMSE}\epsilon_{xy}$
Exponential	0.025000	0.200000	0.058212	0.080463	0.010000	0.054139	0.026067	0.022840	0.087256
Gaussian	0.050000	0.050000	0.062807	0.050000	0.050000	0.064686	0.050000	0.050000	0.116640
Spherical	0.033994	0.094345	0.054454	0.094217	0.042965	0.053718	0.058108	0.059622	0.080574
Matern ($\nu = 3/2$)	0.050000	0.050000	0.058979	0.050000	0.050000	0.059204	0.050000	0.050000	0.094598
Matern ($\nu = 5/2$)	0.050000	0.050000	0.059286	0.050000	0.050000	0.060563	0.050000	0.050000	0.101670

Table B.2
Algorithm results - Sample 12.

	$\theta_{\epsilon_{xx}x}$	$\theta_{\epsilon_{xx}y}$	NRMSE ϵ_{xx}	$\theta_{\epsilon_{yy}x}$	$\theta_{\epsilon_{yy}y}$	NRMSE ϵ_{yy}	$\theta_{\epsilon_{xy}x}$	$\theta_{\epsilon_{xy}y}$	NRMSE ϵ_{xy}
Exponential	0.025000	0.200000	0.058212	0.080463	0.010000	0.054139	0.026067	0.022840	0.087256
Gaussian	0.050000	0.050000	0.062807	0.050000	0.050000	0.064686	0.050000	0.050000	0.116640
Spherical	0.033994	0.094345	0.054454	0.094217	0.042965	0.053718	0.058108	0.059622	0.080574
Matern ($\nu = 3/2$)	0.050000	0.050000	0.058979	0.050000	0.050000	0.059204	0.050000	0.050000	0.094598
Matern ($\nu = 5/2$)	0.050000	0.050000	0.059286	0.050000	0.050000	0.060563	0.050000	0.050000	0.101670

Table B.3
Algorithm results - Sample 13.

	$\theta_{\epsilon_{xx}x}$	$\theta_{\epsilon_{xx}y}$	NRMSE ϵ_{xx}	$\theta_{\epsilon_{yy}x}$	$\theta_{\epsilon_{yy}y}$	NRMSE ϵ_{yy}	$\theta_{\epsilon_{xy}x}$	$\theta_{\epsilon_{xy}y}$	NRMSE ϵ_{xy}
Exponential	0.025000	0.200000	0.038197	0.200000	0.010000	0.058195	0.046934	0.024890	0.065460
Gaussian	0.050000	0.050000	0.041770	0.050000	0.050000	0.061847	0.050000	0.050000	0.069206
Spherical	0.100000	0.200000	0.042714	0.100000	0.200000	0.064990	0.077950	0.06356	0.058844
Matern ($\nu = 3/2$)	0.050000	0.050000	0.037504	0.050000	0.050000	0.059040	0.050000	0.050000	0.060777
Matern ($\nu = 5/2$)	0.050000	0.050000	0.037594	0.050000	0.050000	0.060428	0.050000	0.050000	0.062175

Table B.4
Correlation functions ranking - Sample 21.

	$\theta_{\epsilon_{xx}x}$	$\theta_{\epsilon_{xx}y}$	NRMSE ϵ_{xx}	$\theta_{\epsilon_{yy}x}$	$\theta_{\epsilon_{yy}y}$	NRMSE ϵ_{yy}	$\theta_{\epsilon_{xy}x}$	$\theta_{\epsilon_{xy}y}$	NRMSE ϵ_{xy}
Exponential	0.025000	0.200000	0.069109	0.057017	0.014785	0.061239	0.024489	0.030433	0.065320
Gaussian	0.050000	0.050000	0.088935	0.050000	0.050000	0.091345	0.050000	0.050000	0.087095
Spherical	0.034306	0.14248	0.060205	0.092498	0.052369	0.058183	0.060010	0.066190	0.061712
Matern ($\nu = 3/2$)	0.050000	0.050000	0.077357	0.050000	0.050000	0.067904	0.050000	0.050000	0.068057
Matern ($\nu = 5/2$)	0.050000	0.050000	0.080511	0.050000	0.050000	0.074179	0.050000	0.050000	0.071636

Table B.5
Correlation functions ranking - Sample 22.

	$\theta_{\epsilon_{xx}x}$	$\theta_{\epsilon_{xx}y}$	NRMSE ϵ_{xx}	$\theta_{\epsilon_{yy}x}$	$\theta_{\epsilon_{yy}y}$	NRMSE ϵ_{yy}	$\theta_{\epsilon_{xy}x}$	$\theta_{\epsilon_{xy}y}$	NRMSE ϵ_{xy}
Exponential	0.025000	0.200000	0.027136	0.089675	0.032531	0.030694	0.070711	0.100000	0.034930
Gaussian	0.050000	0.050000	0.019539	0.050000	0.050000	0.025319	0.050000	0.050000	0.030105
Spherical	0.100000	0.200000	0.032513	0.100000	0.200000	0.030760	0.100000	0.200000	0.035440
Matern ($\nu = 3/2$)	0.050000	0.050000	0.022545	0.050000	0.050000	0.026112	0.050000	0.050000	0.028381
Matern ($\nu = 5/2$)	0.050000	0.050000	0.019941	0.050000	0.050000	0.025610	0.050000	0.050000	0.028176

Table B.6
Correlation functions ranking - Sample 23.

	$\theta_{\epsilon_{xx}x}$	$\theta_{\epsilon_{xx}y}$	NRMSE ϵ_{xx}	$\theta_{\epsilon_{yy}x}$	$\theta_{\epsilon_{yy}y}$	NRMSE ϵ_{yy}	$\theta_{\epsilon_{xy}x}$	$\theta_{\epsilon_{xy}y}$	NRMSE ϵ_{xy}
Exponential	0.025000	0.200000	0.030714	0.068302	0.028224	0.050303	0.038192	0.063453	0.038518
Gaussian	0.050000	0.050000	0.027816	0.050000	0.050000	0.056603	0.050000	0.050000	0.043199
Spherical	0.038555	0.41771	0.031087	0.097990	0.068265	0.047713	0.075458	0.123180	0.038287
Matern ($\nu = 3/2$)	0.050000	0.050000	0.028393	0.050000	0.050000	0.051008	0.050000	0.050000	0.038579
Matern ($\nu = 5/2$)	0.050000	0.050000	0.027849	0.050000	0.050000	0.052161	0.050000	0.050000	0.039593

Table B.7
Correlation functions ranking - Sample 31.

	$\theta_{\epsilon_{xx}x}$	$\theta_{\epsilon_{xx}y}$	NRMSE ϵ_{xx}	$\theta_{\epsilon_{yy}x}$	$\theta_{\epsilon_{yy}y}$	NRMSE ϵ_{yy}	$\theta_{\epsilon_{xy}x}$	$\theta_{\epsilon_{xy}y}$	NRMSE ϵ_{xy}
Exponential	0.025000	0.200000	0.019014	0.070711	0.100000	0.018084	0.025000	0.200000	0.020885
Gaussian	0.050000	0.050000	0.012125	0.050000	0.050000	0.016753	0.050000	0.050000	0.019610
Spherical	0.100000	0.200000	0.019364	0.100000	0.200000	0.018071	0.100000	0.200000	0.019591
Matern ($\nu = 3/2$)	0.050000	0.050000	0.014518	0.050000	0.050000	0.016471	0.050000	0.050000	0.017113
Matern ($\nu = 5/2$)	0.050000	0.050000	0.012415	0.050000	0.050000	0.017766	0.050000	0.050000	0.017610

Table B.8
Correlation functions ranking - Sample 32.

	$\theta_{\epsilon_{xx}x}$	$\theta_{\epsilon_{xx}y}$	NRMSE ϵ_{xx}	$\theta_{\epsilon_{yy}x}$	$\theta_{\epsilon_{yy}y}$	NRMSE ϵ_{yy}	$\theta_{\epsilon_{xy}x}$	$\theta_{\epsilon_{xy}y}$	NRMSE ϵ_{xy}
Exponential	0.010000	0.057009	0.052121	0.2000	0.010000	0.057011	0.030858	0.023618	0.051444
Gaussian	0.050000	0.050000	0.055088	0.0500	0.050000	0.051421	0.050000	0.050000	0.057104
Spherical	0.036424	0.082288	0.048601	0.1099	0.050034	0.051750	0.065459	0.059219	0.046153
Matern ($\nu = 3/2$)	0.050000	0.050000	0.052904	0.0500	0.050000	0.052287	0.050000	0.050000	0.049999
Matern ($\nu = 5/2$)	0.050000	0.050000	0.052998	0.0500	0.050000	0.051603	0.050000	0.050000	0.052623

Table B.9
Correlation functions ranking - Sample 33.

	$\theta_{\epsilon_{xx}x}$	$\theta_{\epsilon_{xx}y}$	NRMSE ϵ_{xx}	$\theta_{\epsilon_{yy}x}$	$\theta_{\epsilon_{yy}y}$	NRMSE ϵ_{yy}	$\theta_{\epsilon_{xy}x}$	$\theta_{\epsilon_{xy}y}$	NRMSE ϵ_{xy}
Exponential	0.025000	0.200000	0.058212	0.080463	0.010000	0.054139	0.026067	0.022840	0.087256
Gaussian	0.050000	0.050000	0.062807	0.050000	0.050000	0.064686	0.050000	0.050000	0.116640
Spherical	0.033994	0.094345	0.054454	0.094217	0.042965	0.053718	0.058108	0.059622	0.080574
Matern ($\nu = 3/2$)	0.050000	0.050000	0.058979	0.050000	0.050000	0.059204	0.050000	0.050000	0.094598
Matern ($\nu = 5/2$)	0.050000	0.050000	0.059286	0.050000	0.050000	0.060563	0.050000	0.050000	0.101670

References

- [1] W. He, K. Chen, B. Zhang, K. Dong, Improving measurement accuracy of Brazilian tensile strength of rock by digital image correlation, *Rev. Sci. Instrum.* 89 (11) (2018) 115107, doi:10.1063/1.5065541.
- [2] T.A.C.E. Munoz H, Pre-peak and post-peak rock strain characteristics during uniaxial compression by 3D digital image correlation, *Rock Mech. Rock Eng.* 49 (2016) 2541–2554, doi:10.1007/s00603-016-0935-y.
- [3] H. Song, H. Zhang, D. Fu, Y. Kang, G. Huang, C. Qu, Z. Cai, Experimental study on damage evolution of rock under uniform and concentrated loading conditions using digital image correlation, *Fatigue Fract. Eng. Mater. Struct.* 36 (8) (2013) 760–768, doi:10.1111/ffe.12043. <https://onlinelibrary.wiley.com/doi/abs/10.1111/ffe.12043>
- [4] J. Dautriat, M. Bornert, N. Gland, A. Dimanov, J. Raphanel, Localized deformation induced by heterogeneities in porous carbonate analysed by multi-scale digital image correlation, *Tectonophysics* 503 (1) (2011) 100–116, doi:10.1016/j.tecto.2010.09.025. Thermo-Hydro-Chemo-Mechanical Couplings in Rock Physics and Rock Mechanics
- [5] H. Zhang, G. Huang, H. Song, Y. Kang, Experimental investigation of deformation and failure mechanisms in rock under indentation by digital image correlation, *Eng. Fract. Mech.* 96 (2012) 667–675, doi:10.1016/j.engfracmech.2012.09.012. <https://www.sciencedirect.com/science/article/pii/S0013794412003670>
- [6] H. Xing, Q. Zhang, D. Ruan, S. Dehkoda, G. Lu, J. Zhao, Full-field measurement and fracture characterisations of rocks under dynamic loads using high-speed three-dimensional digital image correlation, *Int. J. Impact Eng.* 113 (2018) 61–72, doi:10.1016/j.ijimpeng.2017.11.011. <https://www.sciencedirect.com/science/article/pii/S0734743X17305018>
- [7] F. Latief, B. Biswal, U. Fauzi, R. Hilfer, Continuum reconstruction of the pore scale microstructure for Fontainebleau sandstone, *Physica A Stat. Mech. Appl.* 389 (8) (2010) 1607–1618, doi:10.1016/j.physa.2009.12.006. <https://www.sciencedirect.com/science/article/pii/S0378437109010024>
- [8] M.S. Talukdar, O. Torsæter, M.A. Ioannidis, J.J. Howard, Stochastic reconstruction, 3D characterization and network modeling of chalk, *J. Pet. Sci. Eng.* 35 (2002) 1–21.
- [9] P. Yin, G.-F. Zhao, Stochastic reconstruction of Gosford sandstone from surface image, *Int. J. Rock Mech. Min. Sci.* 70 (2014) 82–89, doi:10.1016/j.ijrmms.2014.04.012. <https://www.sciencedirect.com/science/article/pii/S1365160914001075>
- [10] A. Henningson, J. Hendriks, Intragranular strain estimation in far-field scanning X-ray diffraction using a Gaussian process, *J. Appl. Crystallogr.* 54 (4) (2021) 1057–1070, doi:10.1107/s1600576721005112.
- [11] A. Gregg, J. Hendriks, C. Wensrich, N. O'Dell, Radial basis functions and improved hyperparameter optimisation for Gaussian process strain estimation, *Nucl. Instrum. Methods Phys. Res. Sect. B Beam Interact. Mater. Atoms* 480 (2020) 67–77, doi:10.1016/j.nimb.2020.08.003. <https://www.sciencedirect.com/science/article/pii/S0168583X20303657>
- [12] C. Jidling, J. Hendriks, N. Wahlström, A. Gregg, T.B. Schön, C. Wensrich, A. Wills, Probabilistic modelling and reconstruction of strain, *Nuclear Instrum. Methods Phys. Res. Sect. B Beam Interact. Mater. Atoms* 436 (2018) 141–155, doi:10.1016/j.nimb.2018.08.051. <https://www.sciencedirect.com/science/article/pii/S0168583X1830524X>
- [13] F. Pierron, M. Grédiac, *The Virtual Fields Method: Extracting Constitutive Mechanical Parameters from Full-field Deformation Measurements*, Springer, New York, 2012.
- [14] F.L. Schwab, Sedimentary petrology, in: R.A. Meyers (Ed.), *Encyclopedia of Physical Science and Technology* (Third Edition), third ed., Academic Press, New York, 2003, pp. 495–529, doi:10.1016/B0-12-227410-5/00678-5. <https://www.sciencedirect.com/science/article/pii/B0122274105006785>
- [15] M.A. Sutton, J.-J. Orteu, H.W. Schreier, *Image Correlation for Shape, Motion and Deformation Measurements: Basic Concepts, Theory and Applications*, Springer, 2009.
- [16] N. McCormick, J. Lord, Digital image correlation, *Mater. Today* 13 (12) (2010) 52–54, doi:10.1016/S1369-7021(10)70235-2.
- [17] E. Jones, M. Iadicola, *A Good Practices Guide for Digital Image Correlation*, International Digital Image Correlation Society, 2018, doi:10.32720/gpg.ed1.
- [18] D.G. Krige, *A statistical approach to some mine valuation and allied problems on the Witwatersrand*, University of the Witwatersrand, South Africa, 1951 Master's thesis.
- [19] G. Matheron, Principles of geostatistics, *Econ. Geol.* 58 (8) (1963) 1246–1266, doi:10.2113/gsecongeo.58.8.1246.
- [20] N.A.C. Cressie, *Statistics for Spatial Data*, John Wiley & Sons Inc., 1993.
- [21] P. Goovaerts, *Geostatistics for Natural Resources Evaluation*, Oxford University Press, 1997.
- [22] M.A. Oliver, R. Webster, *Basic Steps in Geostatistics: The Variogram and Kriging*, Springer.
- [23] T. Cui, D. Pagendam, M. Gilfedder, Gaussian process machine learning and Kriging for groundwater salinity interpolation, *Environ. Model. Softw.* 144 (2021) 105170, doi:10.1016/j.envsoft.2021.105170.
- [24] J. Sacks, W.J. Welch, T.J. Mitchell, H.P. Wynn, Design and analysis of computer experiments, *Stat. Sci.* 4 (1989) 409–435.
- [25] C.E. Rasmussen, C.K.I. Williams, *Gaussian Processes for Machine Learning*, Adaptive Computation and Machine Learning, internet ed., MIT Press Ltd, Cambridge, Massachusetts, 2006.
- [26] V. Dubourg, *Adaptive surrogate models for reliability analysis and reliability-based design optimization*, Université Blaise Pascal, Clermont-Ferrand, France, 2011 Ph.D. thesis.
- [27] T.J. Santner, B.J. Williams, W.I. Notz, *The Design and Analysis of Computer Experiments*, Springer, New York, 2003.
- [28] J.P.C. Kleijnen, *Design and Analysis of Simulation Experiments*, Springer.
- [29] S.N. Lophaven, H.B. Nielsen, J. Søndergaard, DACE - a matlab Kriging toolbox, 2002, <http://www2.compute.dtu.dk/pubdb/pubs/1460-full.html>.
- [30] V. Dubourg, B. Sudret, J.-M. Bourinet, Reliability-based design optimization using Kriging surrogates and subset simulation, *Struct. Multidiscip. Optim.* 44 (5) (2011) 673–690, doi:10.1007/s00158-011-0653-8.
- [31] C. Lataniotis, D. Wicaksono, S. Marelli, B. Sudret, UQLab user Manual - Kriging (Gaussian Process Modeling), Technical Report UQLab-V2.0-105, Chair of Risk, Safety and Uncertainty Quantification, ETH Zurich, Switzerland, 2022.
- [32] S.J. Matthews, *Speckle pattern control in the application of digital image correlation for detecting damage in helmets*, University of Surrey, 2020 Ph.D. thesis.